

<sup>1</sup> Hybridisation of volume of fluid, pore network, and continuum  
<sup>2</sup> Darcy models for simulating multi-scale multi-physics flow in coal

<sup>3</sup> Zakhar Lanetc<sup>a,\*</sup>, Aleksandr Zhuravljov<sup>b</sup>, Peyman Mostaghimi<sup>a</sup>

<sup>4</sup> <sup>a</sup>*School of Minerals and Energy Resources Engineering, University of New South Wales, Sydney, NSW 2052, Australia*

<sup>5</sup> <sup>b</sup>*Institute of Environmental and Agricultural Biology, University of Tyumen, Tyumen 625003, Russia*

---

<sup>6</sup> **Abstract**

It is a challenging task to predict and analyse the transient flow physics in unconventional complex geological formations such as coal seams. This is due to the multi-scale multi-physics nature of processes taking place in coal seam gas reservoirs. Therefore, numerical tools allowing the incorporation of various flow physics inherent to coal into the simulation routine are of particular importance. At the pore-scale, the flow modelling in multi-scale porous and fractured media is typically conducted with the aid of direct numerical simulations (Lattice Boltzmann method or by solving Navier Stokes equations) or by utilising so-called pore-network modelling. Both methods have advantages and drawbacks while their hybridisation may allow to avoid some of the major pitfalls. In this work, we develop a hybrid numerical model which combines the Hagen–Poiseuille analytical solution and the volume of fluid advection scheme for fluid flow in fractures with the continuum Darcy flow in the coal matrix. The explicit coupling of fluid flow across the fracture-matrix domains is implemented via the corresponding source terms in the governing equations. Besides, the additional multi-physics including sorption and matrix swelling-shrinkage phenomena are also introduced into the numerical scheme of the developed model. The hybrid solver is validated against available analytical solutions and the previously developed Darcy-Brinkman-Stokes framework which has similar functionality with respect to modelling fluid flow in coal seams. To validate the developed model and show its capability to capture multi-scale multi-physics flow physics in coal, several illustrative simulations are conducted using synthetic and realistic digital images of coal. As a result, the accuracy of the hybrid solver was within 4% when compared to the Darcy-Brinkman-Stokes framework with respect to the flow simulation on realistic geometry. Besides, the non-parallelised hybrid model outperformed the parallelised direct numerical simulation being more than 40 times faster in computational time. The findings are beneficial for conducting larger core-scale simulations of

multi-scale multi-physics flow in coal seams with potential applications to natural gas production, hydrogen storage and  $CO_2$  sequestration.

- 7    *Keywords:* Pore network modelling, Volume of fluid method, Darcy model, Transient  
8    multiphase flow, Fractured multi-scale media, Multi-physics
- 

9    **1. Introduction**

10    Coal seams are abundant with natural gas, predominately methane ( $CH_4$ ) with smaller quantities of other gases including carbon dioxide ( $CO_2$ ), nitrogen ( $N_2$ ) and ethane ( $C_2H_6$ ) and no natural-gas condensate [1, 2]. Gases in coal seams are generally formed during coalification when kerogen and organic matter are converted into coal [3, 4]. Unlike conventional gas formations, coal seam gas (CSG) is stored within the coal matrix in an absorbed near-liquid state while open fractures are initially saturated with formation water [5, 6, 7].

16    This natural resource was initially produced as a safety measure in order to vent methane out of "gassy" coal beds before mining commencement [8, 9]. Subsequently, CSG became economically producible as an independent natural-gas resource in the US, Australia, Canada, China and India [10, 11, 12, 13]. Considering the current global climate agenda, there are also potential environmental benefits associated with CSG production. For instance,  $CO_2$  sequestration into unmineable coal formations may not only enhance  $CH_4$  recovery but also aid in mitigating the emissions of  $CO_2$  greenhouse gas [14, 15, 16]. Likewise, coal seam formations are currently considered as one of the most suitable options for hydrogen storage [17, 18].

24    Since coal is mainly carbon-based, CSG reservoirs behave in a fundamentally distinctive way compared to so-called conventional limestone or sandstone gas reservoirs. For instance, coal permeability is highly influenced by the stress regime due to high coal compressibility [19, 20]. Moreover, the dual-porosity nature of coal along with its sorption capacity makes the characterisation of CSG reservoirs challenging by rising the level of uncertainty [3, 21]. Thus, it is essential to develop numerical tools which would allow gaining deeper insights regarding the multi-physics and multi-scale transport in coal. These methods should allow to quantify and reduce the uncertainty and thus risk of CSG exploration programmes.

---

\*Corresponding author

Email addresses: z.lanetc@unsw.edu.au (Zakhar Lanetc), a.s.zhuravljov@gmail.com (Aleksandr Zhuravljov), peyman@unsw.edu.au (Peyman Mostaghimi)

Preprint submitted to To be decided

October 1, 2022

32 It is arguably easier to analyse multi-physics processes when operating on a pore-scale and  
33 directly considering the interplay between various flow phenomena on a physical level. There are  
34 two most frequently used approaches to conduct pore-scale flow simulations, namely pore-network  
35 modelling (PNM) [22, 23, 24, 25] and direct numerical simulations (DNS) [26, 27, 28, 29, 30].  
36 Both PNM and DNS methods allow to utilise so-called image-based modelling (IBM) [31] and  
37 conduct the simulation on the underlying micro-CT images [32, 33]. While DNS can be directly  
38 conducted on the segmented micro-CT images, PNM would require additional pre-processing.  
39 Such pre-processing is called pore-network extraction and uses the segmented micro-CT images  
40 to geometrically simplify porous medium to the form of an artificial network [34, 35, 36].

41 Since coal is highly heterogeneous and its matrix consists mainly of micropores ( $< 2 \text{ nm}$ )  
42 and mesopores (2-50 nm) [37] and due to the limited resolution of modern micro-CT equipment,  
43 there will always be not individually resolved regions when segmenting coal micro-CT images.  
44 Nevertheless, such sub-resolved regions have to be accounted for during CSG flow simulations  
45 since most of the gas reserves are held and transported within the coal matrix [38, 39, 40]. In  
46 PNM, this issue was addressed by introducing multi-scale pore networks (PNs) where micro-  
47 porosity can be presented by additional fine-scale PNs or artificial hydraulic links in-between  
48 macro-scale PN elements [41, 42]. The accuracy of this approach in predicting the connectivity  
49 of micro-porous regions is questionable due to the high uncertainty when choosing the features  
50 of fine-scale network topology [43, 44].

51 An alternative way to account for multi-scale flow in dual-porosity systems containing sub-  
52 resolved regions is so-called the Micro-Continuum approach [45, 46]. This approach utilises  
53 the Darcy-Brinkman-Stokes (DBS) method to couple flow in resolved and sub-resolved regions  
54 by introducing the Darcy flow component into the volume of fluid (VOF) numerical technique  
55 [47, 48]. A DBS model of flow in dual-porosity media asymptotically approaches Darcy's  
56 component in sub-resolved regions and Navier-Stokes equations (NSE) in the resolved void space  
57 [43, 49]. There are a number of works which utilise the DB method to account for the flow  
58 in dual-porosity systems [50, 51, 52, 53]. Despite DBS simulations allow greatly reducing  
59 the uncertainties of multi-scale PNM, there are high computational costs associated with this  
60 approach, especially when approaching the representative elementary volume (REV).

61 In CSG, it is not enough to only account for multi-scale multiphase flow as other phenomena  
62 should also be considered when conducting numerical simulations. Thanks to the complex multi-

63 physics processes associated with coal that include sorption, diffusion, deformation and reactive  
64 transport [54, 55, 56, 57, 58]. Both PNM and DBS methods have been utilised to account for  
65 some of these multi-physics processes. However, this was mainly done concerning shale rocks  
66 that can be characterised by similar multi-physics as coal.

67 In PNM, the multi-physics processes are commonly accounted for by combining transport  
68 (advection and diffusion) and sorption terms into a single mathematical model [59, 60, 61]. The  
69 variation in channel dimensions due to sorption is then predicted to account for the change of  
70 pressure gradient and velocity fields during multi-physics simulations. However, most of the  
71 developed models operate only in the micro-porous regions and omit the flow in open fractures  
72 [62, 63, 64]. Lanetc et al. (2020) [65] coupled Fick's second law, the empirical Langmuir isotherm  
73 and fracture PN to simulate the sorption, transient gas flow in the coal matrix and through coal  
74 fractures simultaneously. Similar phenomena were included in the research conducted by Jing  
75 et al. (2020) [66] where both micro-porosity and fractures were presented by PNs of different  
76 scales. Nevertheless, both these models have only considered a gas phase and neglected the  
77 multi-phase nature (water-gas) associated with flow in coals.

78 In DNS, the DBS method is actively utilised as a platform for the incorporation of various  
79 multi-physics processes including reactive transport and deformable media [67, 68, 69, 70].  
80 Moreover, Soulaine et. al. (2019) developed a DB framework to account for various nano-scale  
81 mechanisms related to shale such as Knudsen and surface diffusion, sorption and Klinkenberg  
82 gas slippage effect. In this work, diffusion and sorption multi-physics were introduced within a  
83 Darcy DBS component through Fick's second law, the Langmuir equation, and a source term in  
84 the continuity equation. Likewise, Lanetc et al. [71] adapted the DBS approach to simulate the  
85 multi-physics phenomena taking place in coal by incorporating sorption, surface diffusion, gas  
86 and rock compressibility, as well as sorption-induced swelling into the DB framework. In contrast  
87 with Soulaine et. al. (2019), this work incorporates the multi-physics phenomena by considering  
88 the source term as pressure-dependent within an implicit numerical scheme. Nevertheless, all  
89 the multi-physics extensions of the DB approach inherent the high computation costs associated  
90 with this method.

91 Following the above discussion, there is a need to develop hybrid approaches allowing to  
92 combine the computational efficiency of PNM with the accuracy of DNS methods. In our previous  
93 research papers [72, 73], we already coupled network modelling and volume of fluid methods for

94 multiphase flow in open fractures and demonstrated the applicability and computational efficiency  
 95 of a hybrid VOF-PNM model for various transient multiphase displacement scenarios. However,  
 96 this model fully overlooked the flow in a coal matrix which should be considered in most of  
 97 CSG simulations. Thus, this paper aims to develop the hybrid VOF-PNM-Darcy solver for the  
 98 simulation of transient multi-physics phenomena in coal fractures (VOF-PNM) and matrix (Darcy)  
 99 simultaneously. The incorporated into the model multi-physics processes include multi-phase  
 100 (water-gas) flow in deformable fractures and in the matrix, as well as sorption. The proposed  
 101 numerical approach has similar functionality to the previously developed DBS framework for  
 102 coal but significantly surpasses it in terms of computational efficiency.

## 103 2. Methods

104 The proposed mathematical model is dedicated to quasi-one-dimensional (1D, PN-based)  
 105 two-phase incompressible flow in pore and continuum scales. Throats of such PN represent  
 106 coal fractures (pore-scale), while the coal matrix is simulated using a set of one-dimensional  
 107 Darcy-type extra domains (continuum scale). The interaction between the scales is provided by  
 108 the correspondent source terms introduced in the governing equations.

109 Regarding pore-scale, each throat in the network is discretised via 1D Finite Volume Method  
 110 (FVM) while junctions of the throats are treated throughout the non-neighbour connections. The  
 111 velocity between neighbouring grid blocks is calculated using the modified Hagen–Poiseuille  
 112 equation:

$$v^{n+1} = -\frac{\bar{K}}{\bar{\mu}^n} \left( \frac{\Delta P^{n+1}}{\Delta L} + \frac{\Delta P_c^n}{\Delta L} \right), \quad (1)$$

113 where  $n$  is a particular discrete moment in time,  $\bar{K}$  is the average conductance of the neighbouring  
 114 grid blocks,  $\bar{\mu}$  is average dynamic viscosity, while  $\Delta L$  is the distance between centres of the  
 115 neighbouring grid blocks.  $\Delta P$  and  $\Delta P_c$  are pressure difference and capillary pressure drop  
 116 between the neighbouring grid blocks, respectively. The sign of  $\Delta P$  and  $\Delta P_c$  is defined by a  
 117 relative face orientation between the grid blocks. Compared to the conventional PNM methods,  
 118 the employed approach is conceptually close to a single pressure [23], since one pressure  $P$  is  
 119 related to both phases. Furthermore, this approach is similar to the one used in our previous  
 120 manuscripts dedicated to the hybridisation of VOF and PNM methods for multi-phase fluid flow  
 121 in fractures [72, 73]. However, the previously developed VOF-PNM model has not discretised the

<sup>122</sup> fractures with respect to pore pressure calculation and used the pressure values inside the throats'  
<sup>123</sup> nodes to estimate the velocity as it is typically done in conventional PNM implementations.

<sup>124</sup> The conductance  $K$  of 2D and 3D rectangular grid blocks can be calculated as follows [73, 74]:

$$K = \begin{cases} \frac{w^2}{12F_k} : & 2D, \\ \frac{w^2}{12F_k} \left( 1 - \sum_{odd,i}^{\infty} \frac{1}{i^5 \pi^5} \tanh \left( i\pi \frac{h}{2w} \right) \right) : & 3D, \end{cases} \quad (2)$$

<sup>125</sup> where  $w$  and  $h$  are grid block width and height and  $h > w$  with respect to 3D geometry, while  
<sup>126</sup> correction factor  $F_k$  is embedded to account for empirical conductance variation due to matrix  
<sup>127</sup> swelling-shrinkage phenomena using Palmer-Mansoori model (3) [75]:

$$\frac{\phi}{\phi_0} = 1 + \frac{P - P_0}{M\phi_0} + \varepsilon_L \frac{(B - C)}{3\phi_0 C} \left( \frac{P}{P_L + P} - \frac{P_0}{P_L + P_0} \right), \quad (3)$$

<sup>128</sup> where  $\phi_0$  is porosity at pressure  $P_0$ , axial modulus  $C = E \frac{1-\nu}{1+\nu} (1 - 2\nu)$ , where  $E$  is Young's  
<sup>129</sup> modulus and  $\nu$  is Poisson's ratio, bulk modulus  $B = \frac{E}{3} (1 - 2\nu)$ , and  $\varepsilon_L$  is Langmuir volumetric  
<sup>130</sup> strain. Thus, considering porosity  $\phi$  dependent on pressure, the fracture conductance variation  
<sup>131</sup> during the swelling-shrinkage processes can be modelled using the correction factor  $F_k$  [20, 76]:

$$F_k = \left( \frac{\phi_0}{\phi} \right)^m : m = \begin{cases} 2 : & 2D, \\ 3 : & 3D. \end{cases} \quad (4)$$

<sup>132</sup> Consequently, the dynamic viscosity is calculated using saturation of both phases 0 and 1:

$$\mu^n = \mu_0 S_0^n + \mu_1 S_1^n, \quad (5)$$

<sup>133</sup> where  $\mu_0$  and  $\mu_1$  are dynamic viscosities of phases 0 and 1, respectively, while saturations of the  
<sup>134</sup> phases obey the following condition:

$$S_0^n + S_1^n = 1, \quad (6)$$

<sup>135</sup> The capillary pressure drop  $\Delta P_c$  between the neighbouring grid blocks for 2D and 3D  
<sup>136</sup> rectangular cases is defined using interfacial tension  $\beta$  and contact angle  $\theta$  by the following  
<sup>137</sup> equation [72, 73]:

$$\Delta P_c^n = sgn(\Delta S_0^n) |\Delta S_0^n|^\gamma 2\beta \cos\theta \begin{cases} \frac{l}{w} : & 2D, \\ \left( \frac{l}{h} + \frac{l}{w} \right) : & 3D, \end{cases} \quad (7)$$

138 where  $\Delta S_0$  is a saturation difference of phase 0 between the neighbouring grid blocks. The sign  
 139 of  $\Delta S_0$  is defined by a relative face orientation between the grid blocks. Tuning parameter  $\gamma$   
 140 allows for adjusting the absolute value of the capillary pressure drop and can vary depending on  
 141 the flow displacement physics (e.g., drainage or imbibition).

142 The conservation of total volumetric fluxed of both phases for each moment in time can be  
 143 represented by the following steady-sate equation:

$$\sum_{\Delta\Omega} v^{n+1} \Delta\Omega - (q_0^n + q_1^n) \Delta V = 0, \quad (8)$$

144 where  $\Delta\Omega$  represents the faces of a particular grid block and  $\Delta V$  is its volume, while  $q_0$  and  $q_1$   
 145 are the volumetric flux densities due to source. The sign of face  $\Delta\Omega$  is defined by its relative  
 146 orientation. Substitution of Eq. (1) into Eq. (8) results in the following equation for pressure  $P$ :

$$-\sum_{\Delta\Omega} \frac{\bar{K}}{\mu^n} \frac{\Delta P^{n+1}}{\Delta L} \Delta\Omega - \sum_{\Delta\Omega} \frac{\bar{K}}{\mu^n} \frac{\Delta P_c^n}{\Delta L} \Delta\Omega - (q_0^n + q_1^n) \Delta V = 0. \quad (9)$$

147 In this equation, the boundary conditions (BC) can be implemented differently: (1) Dirichlet type  
 148 BC can be imposed on all boundary faces and (2) mixed BC can be implemented where both  
 149 Dirichlet and Neumann type BC are imposed on different boundary faces.

150 While the velocity can be calculated by solving Eq. (9), the saturation distribution can be  
 151 estimated by employing the transient equation which represents the conservation of volumes for  
 152 phase 0:

$$\frac{S_0^{n+1} - S_0^n}{\Delta t} \Delta V + \sum_{\Delta\Omega} v^{n+1} \bar{S}_0^{n+1} \Delta\Omega - q_0^n \Delta V = 0, \quad (10)$$

153 where  $\Delta t$  is the numerical time step and  $\bar{S}_0$  is saturation interpolated by the 'upwind' method [77].  
 154 The BC that can be implemented in Eq. (10) are similar to the ones described above regarding  
 155 Eq. (9). Although, considering Eq. (10), the Neumann type BC should not contradict with Eqs. (1)  
 156 and (6). Besides, the numerical solution of Eqs. (9) and (10) is implemented sequentially.

157 The Darcy 1D model is employed for incompressible two-phase transport in continuum  
 158 porous media (non-resolved matrix) via SEQ method [77], while the Langmuir isotherm is used  
 159 to simulate the sorption process [55, 78, 79]. The equation responsible for the conservation of  
 160 volume regarding continuum scale is given below:

$$\int_V \frac{\partial \phi S_i}{\partial t} dV + \oint_{\Omega} \phi S_i v_i d\Omega = \int_V \tilde{q}_i dV, \quad (11)$$

161 where  $i$  denotes phase ( $0$  or  $1$ ),  $\phi$  is matrix porosity,  $\Omega$  is area,  $t$  is time, and  $\tilde{q}_I$  is volumetric  
 162 flux density of phase  $I$  due to sorption. The following equation represents the two-phase Darcy  
 163 model, which implies the proportionality between velocity and pressure gradient for a particular  
 164 phase:

$$\phi S_i v_i = -\frac{k_{ri} k}{\mu_i} \frac{\partial P_i}{\partial x}, \quad (12)$$

165 where  $k$  and  $k_r$  are absolute and relative permeabilities of matrix, respectively. Since this model  
 166 contains distinctive pressures for each of the phases, capillary pressure difference  $P_c$  can be  
 167 expressed explicitly as follows:

$$P_I - P_0 = P_c. \quad (13)$$

168 Flow characteristics of the continuum model such as absolute permeability  $k$ , relative perme-  
 169 ability  $k_{ri}$  and capillary pressure  $P_c$  are defined by the Brooks-Corey correlations [80, 81]:

$$\begin{aligned} k_{r0} &= A_0 \left( \frac{S_0 - S_{0r}}{1 - S_{0r} - S_{Ir}} \right)^{m_0}, \\ k_{Ir} &= A_I \left( \frac{1 - S_0 - S_{Ir}}{1 - S_{0r} - S_{Ir}} \right)^{m_I}, \\ P_c &= A_c \left( \frac{S_0 - S_{0r}}{1 - S_{0r} - S_{Ir}} \right)^{-m_c}, \end{aligned} \quad (14)$$

170 where  $A_i, A_c, S_{ir}, m_i, m_c$  are Brooks-Corey correlation parameters.

171 Furthermore, to keep this continuum-scale model in agreement with the pore-scale constitute  
 172 of the hybrid model, the following notation is introduced:

$$P = P_0 S_0 + P_I S_I. \quad (15)$$

173 By employing such notation, the volumetric flux densities  $\tilde{q}_I$  can be numerically expressed as  
 174 follows:

$$\tilde{q}_I = \alpha' \frac{\partial P}{\partial t}, \quad (16)$$

175 where  $\alpha = \alpha(P)$  is the Langmuir isotherm which provides equilibrium volume concentration of  
 176 the adsorbed phase  $I$ ,  $\alpha' = \frac{d\alpha}{dP}$  and it is assumed that  $\frac{\partial P}{\partial t} \gg \frac{\partial P}{\partial x} \frac{dx}{dt}$ :

$$\alpha = \frac{\alpha_L P}{P_L + P} \quad (17)$$

177 where  $\alpha_L$  and  $P_L$  are the Langmuir constants.

178        As it follows from Eq. (12), the continuum scale mathematical model is 1D. The coupling with  
 179        the pore-scale model is implemented explicitly through the correspondent boundary conditions  
 180        and volumetric flux densities  $q_0$  and  $q_1$  (Eq. (9)) which are treated as additional sources coming  
 181        from the faces of the continuum scale model connected to the fractures' finite volume grid blocks.  
 182        Considering dead-end faces of the continuum scale model, the no-flow boundary condition is  
 183        assigned.

184        The conceptual representation of the hybrid model is depicted in Fig. 1. In Fig. 1a, a  
 185        segmented micro-CT image of resolved fractures is surrounded by a non-resolved coal matrix. In  
 186        turn, Fig. 1b demonstrates how the surrounded matrix volumes are treated in the 'HybridPNM'  
 187        solver by artificially introduced matrix elements. The total volume of such elements is equal to  
 188        the matrix volume of the realistic micro-CT image. The main challenge is to relevantly distribute  
 189        the artificial matrix elements amongst the fractures. The algorithm implemented in this study  
 190        implies that the volume of the matrix elements adjacent to the cleats is directly proportional to  
 191        fractures' surfaces. The 'HybridPNM' numerical representation treats the artificial matrices as  
 192        non-overlapping, despite, in reality, the fluids from the same spacial location within the matrix  
 193        can flow into several fractures simultaneously (Fig. 1b).

194        The dimensional numbers reported for some of the conducted simulations in the following  
 195        section 3 are calculated as follows:

$$M = \frac{\mu_0}{\mu_I}, \quad Ca = \frac{\mu^{in} u}{\sigma}, \quad (18)$$

196        where  $M$  and  $Ca$  are viscosity ratio and capillary number, respectively, while  $\mu^{in}$  is viscosity at  
 197        the sample inlet, and  $u$  is an average velocity concerning entire the pore-scale model.

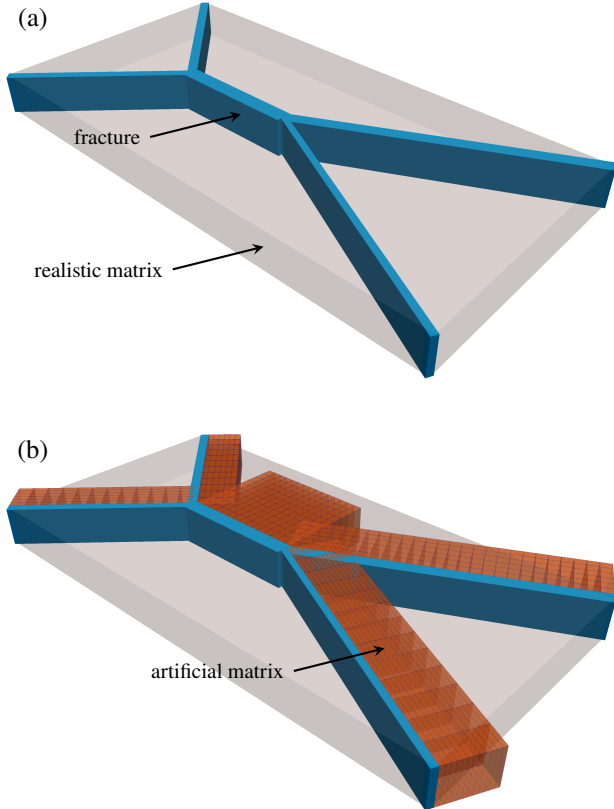


Figure 1: Schematic representation of (a) an arbitrary fractured image, (b) the same model with adjacent artificial matrix elements (applicable for various scales). The total volume of the matrix elements is equal to the real volume of the sample under investigation.

**198 3. Results and Discussion**

**199** In order to scrutinise the developed hybrid solver, we divide this section into three parts.  
**200** Firstly, we validate the flow simulation in open fractures conducted by the 'HybridPNM' solver  
**201** against conventional VOF simulation 'InterFOAM' (Section 3.1). Secondly, we validate the  
**202** Darcy constitute of the 'HybridPNM' model against the analytical Buckley-Leverett solution (Sec-  
**203** tion 3.2). Here we also demonstrate the implementation of the sorption mechanism inside the  
**204** matrix domain. Finally, we conduct several coupled multi-scale multi-physics simulations with  
**205** the 'HybridPNM' solver and compare them against the 'OpenFOAM' based Darcy-Brinkman-  
**206** Stokes framework (Section 3.3).

207    3.1. Flow in open fractures

208    Drainage and imbibition multi-phase simulations are conducted with both 'HybridPNM' and  
 209    VOF solvers inside a simplified 2D channel. The viscosity ratio  $M$  is unity for simplicity while  
 210    the contact angles are  $135^\circ$  and  $45^\circ$  for drainage and imbibition simulations, respectively. The  
 211    Neumann boundary conditions are imposed at the inlet to inject fluid with constant velocity. The  
 212    capillary numbers  $Ca$  for both drainage and imbibition simulations equal  $5 \times 10^{-3}$  to visually  
 213    demonstrate the considerable pressure drop at the fluid interface.

214    In Figs. 2 and 3, the saturation distributions of two liquids at time  $0.51s$  are depicted in  
 215    the 2D channel for both 'HybridPNM' and VOF models with respect to drainage and imbibition  
 216    simulations, respectively. The 2D VOF model employs regular cuboid grid-blocks discretisation,  
 217    while the 1D 'HybridPNM' provides identical to the 2D model distance between grid block  
 218    centres. As a result, the shape of the fluid interface is curved with respect to VOF simulation and  
 219    flat for the 'HybridPNM' model (Figs. 2 and 3).

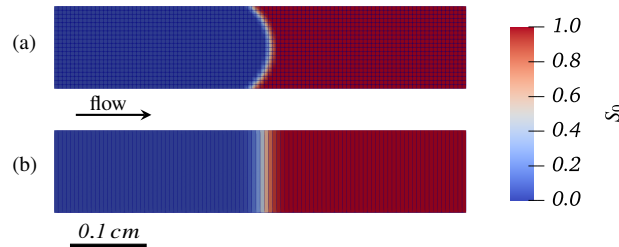


Figure 2: Saturation distribution in a 2D rectangular channel at time  $0.51s$  for (a) VOF and (b) 'HybridPNM' drainage simulations. The contact angle  $\theta$  equals  $135^\circ$  while viscosity ratio  $M$  is 1.

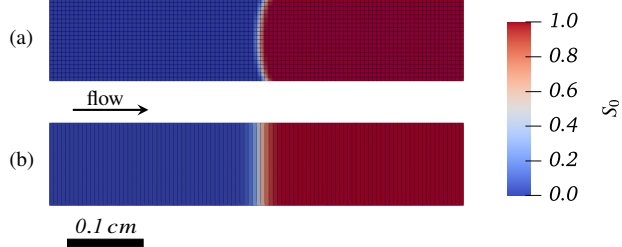


Figure 3: Saturation distribution in a 2D rectangular channel at time  $0.51s$  for (a) VOF and (b) hybridPNM imbibition simulations. The contact angle  $\theta$  equals  $45^\circ$  while viscosity ratio  $M$  is 1.

It is clear that the interface location of 'HybridPNM' and VOF simulations at a particular time will coincide since the constant inlet velocity is imposed by the Neumann-type boundary condition. Therefore, it is essential to analyse the pressure profiles of the 'HybridPNM' and VOF simulations along the channel at a particular moment in time. In Figs. 4 and 5, saturation  $S_0$  and pressure  $P$  profiles at time  $0.51s$  are depicted in 1D for both 'HybridPNM' and VOF models with respect to the drainage and imbibition simulations, respectively. Considering immiscible multi-phase flow physics, there should be a pressure drop at the fluid interface for the drainage displacement and pressure surge for imbibition. This pressure behaviour is explained by the opposite direction of capillary forces for drainage and imbibition cases and is visually observable in VOF simulations by comparing the meniscus curvatures (Figs. 2a and 3a). As can be seen in Figs. 4 and 5, the pressure profiles of 'HybridPNM' and VOF simulations closely coincide along the whole channel length including the location of the fluid interface. This allows us to make the conclusion that the simplified algorithm used in the 'HybridPNM' model with respect to capillary pressure drop provides sufficient accuracy for modelling multiphase flow in open fractures.

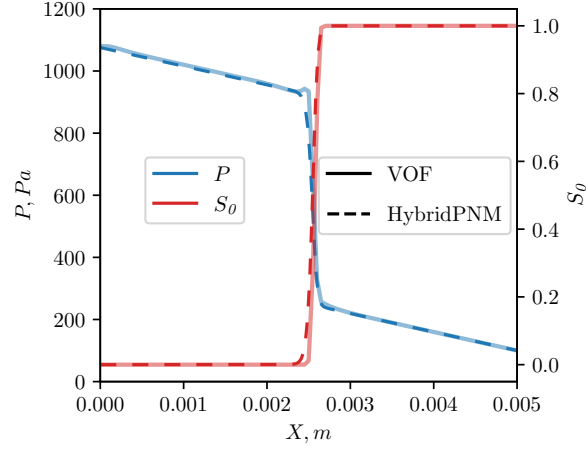


Figure 4: Pressure and saturation profiles along a 2D rectangular channel at time  $0.51s$  for 'HybridPNM' and VOF drainage simulations.

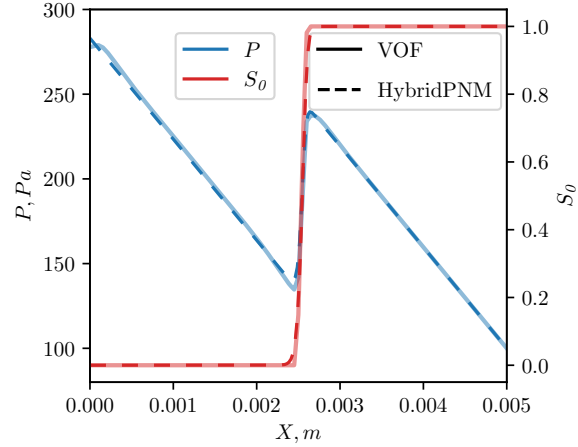


Figure 5: Pressure and saturation profiles along a 2D rectangular channel at time  $0.51s$  for 'HybridPNM' and VOF imbibition simulations.

234    *3.2. Flow in matrix*

235    Since the flow in the matrix domain is modelled through the continuum Darcy model, it is  
236 important to commence with its validation. For this, the analytical Buckley-Leverett solution is  
237 utilised [82, 83, 84]. In the validation case, the length of the 1D model is  $0.1\text{ m}$ , while porosity  
238 and absolute permeability equal  $0.2$  and  $1$  Darcy, respectively. The number of numerical grid

239 blocks used for the simulation by 'HybridPNM' is 2000. The relative permeability curves used  
 240 as an input to both analytical and numerical models are depicted in Fig. 6b. As can be observed  
 241 in Fig. 6a, the analytical and numerical solutions closely match (the numerical error is less than  
 242 0.03%) for all depicted moments in time.

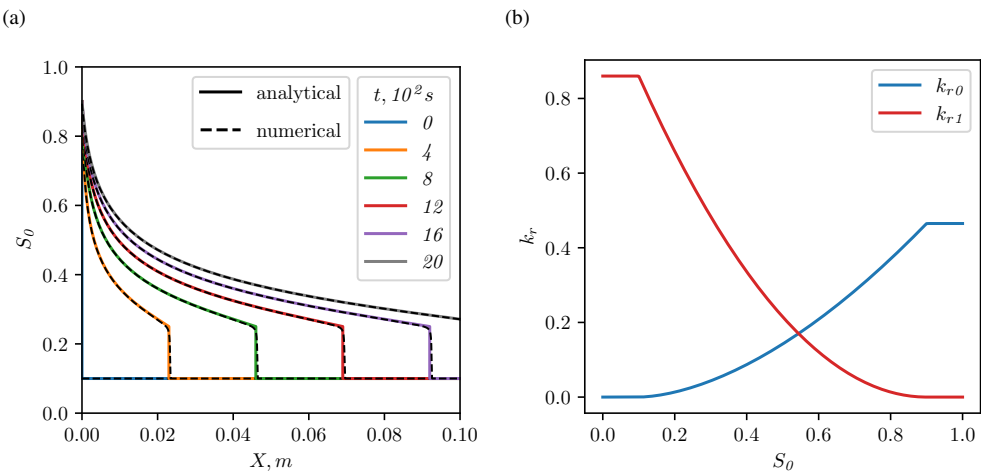


Figure 6: One-dimensional saturation profiles for different times: (a) The developed two-phase Darcy solver and Buckley–Leverett analytical model, (b) Utilised relative permeability curves.

243 Having the Darcy constitute of the 'HybridPNM' model validated with respect to the analytical  
 244 solution of immiscible two-phase flow, the sorption phenomena is further introduced within a  
 245 matrix Darcy domain by utilising the Langmuir equation (17) and the source term in Eq. (11).  
 246 To exemplify sorption effect on two-phase flow characteristics, both desorption and adsorption  
 247 simulations are conducted (Figs. 7 and 8). For these simulations, the model characteristics and  
 248 simulation parameters are the same as the one used for validation with the Buckley-Leverett  
 249 analytical solution. Besides, the sorption isotherm is introduced via the Langmuir constants  $\alpha_L$   
 250 and  $P_L$  (Table 3), respectively.

251 In Fig. 7, the gas release into the matrix occurs due to desorption. The entire domain can be  
 252 identified as a 1D representation of the coal matrix where its left boundary ( $X = 0 m$ ) represents  
 253 the farthest point from the fracture. In contrast, the right boundary ( $X = 0.1 m$ ) is located at  
 254 the hypothetical matrix-fracture adjacency. At initial conditions ( $t = 0$ ), the matrix is saturated  
 255 with water while the free gas is at its irreducible value ( $S_I = 0.1$ ). Likewise, the pressure is

256 uniform ( $1 \text{ MPa}$ ) along the whole matrix and adsorbed gas volume concentration is equal to its  
257 equilibrium concentration (7.4) obtained by the Langmuir isotherm. At the following numerical  
258 time step, the pressure value at the matrix-fracture adjacence (right boundary) is deliberately  
259 dropped by 3% and fixed throughout the rest of the simulation by imposing the Dirichlet type  
260 boundary condition. In turn, the no-flow boundary condition is imposed at the outer face of  
261 the matrix (left boundary). Due to the negative pressure gradient along the matrix length, the  
262 gas phase commences desorbing into a free state within the coal matrix following the drop in  
263 equilibrium concentration estimated by the pressure-dependent Langmuir isotherm. The gas  
264 release into the free state affects the saturation profile inside the matrix since water is getting  
265 replaced by the desorbed gas. As time goes on, the magnitude of the pressure gradient between  
266 the left and right boundaries of the matrix reduces with saturation and volume concentration  
267 profiles responding accordingly.

268 In Fig. 8, the water inflow into the matrix occurs due to adsorption. The simulation setup  
269 with respect to initial and boundary conditions, model geometry and other characteristics of the  
270 adsorption simulation is similar to the desorption case described above and depicted in Fig. 7.  
271 Although, there are two differences. Firstly, at initial conditions, the matrix is filled with gas while  
272 water is at its irreducible value ( $S_0 = 0.1$ ). Secondly, the pressure value is not dropped but raised  
273 by 3% at the matrix-fracture adjacence at the first numerical time step. This results in a positive  
274 pressure gradient between the left and right boundaries and also increases the average pressure  
275 inside the matrix. Such pressure increase affects the equilibrium gas concentration calculated by  
276 the Langmuir isotherm and gas begins to adsorb being displaced by inflowing water. In contrast  
277 with the desorption case, for the adsorption simulation, the adsorbed concentration profile does  
278 not fully follow the pressure distribution with respect to the curves' shape. Such peculiarity can  
279 be observed as some amount of free gas is pushed towards the left boundary of the matrix before  
280 it has time to locally adsorb to its equilibrium concentration.

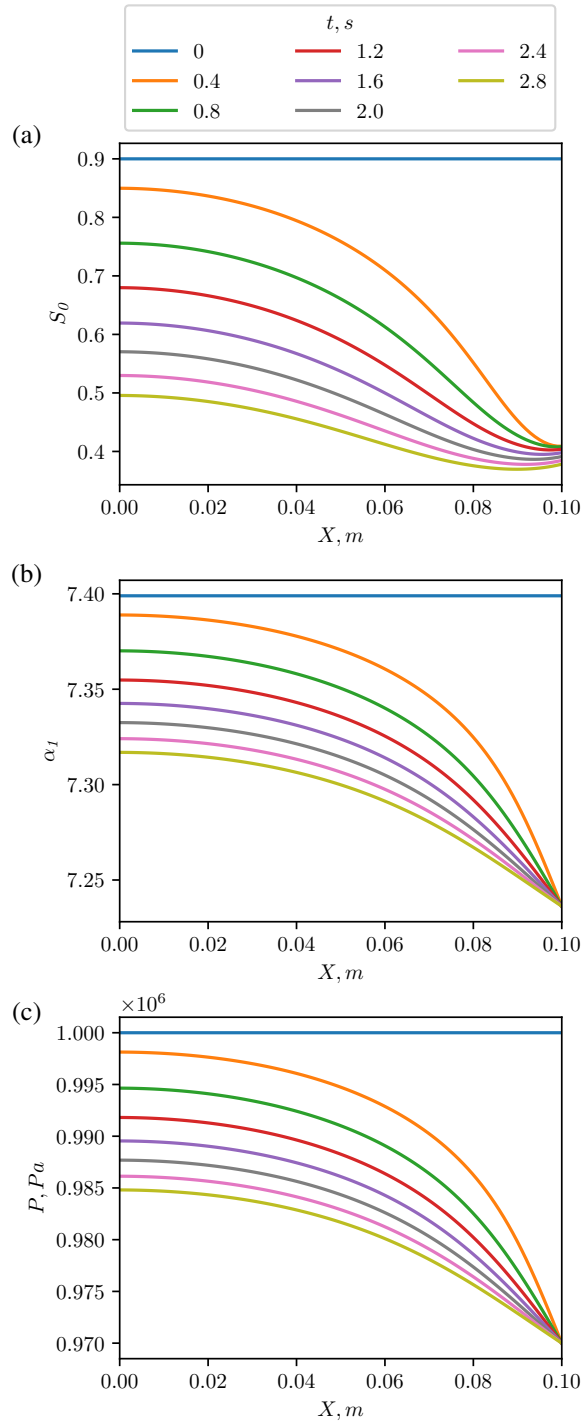


Figure 7: Gas release into matrix due to gas desorption: (a) water saturation, (b) adsorbed gas concentration, (c) pore pressure.

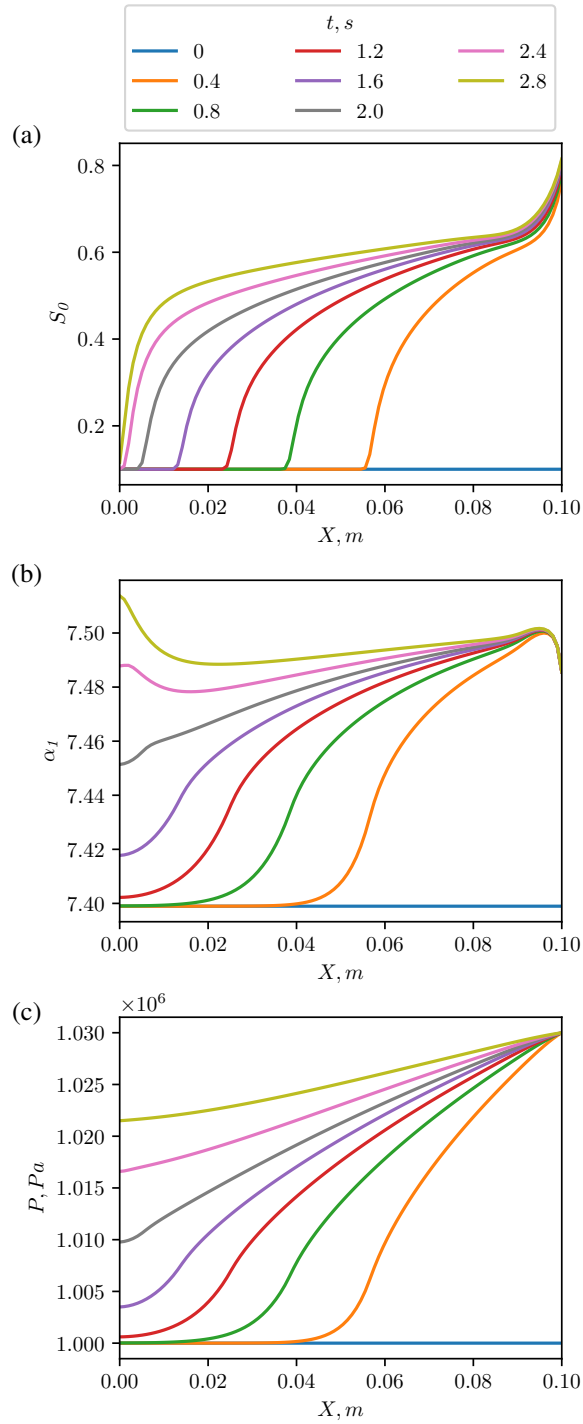


Figure 8: Water inflow into matrix due to gas adsorption: (a) water saturation, (b) adsorbed gas concentration, (c) pore pressure.

281    *3.3. Coupled matrix-fracture system*

282    In order to assess whether the developed 'HybridPNM' model is able to correctly capture  
283    the multi-scale multi-physics phenomena related to coal, we use the previously developed Darcy-  
284    Brinkman-Stokes (DBS) solver for benchmarking [71]. Both 'HybridPNM' and DBS solvers  
285    attempt to capture similar phenomena by coupling resolved fractures with the sub-resolved  
286    matrix domain, although their numerical realisation is different. In 'HybridPNM', the PNM-  
287    based flow in fractures is embedded into the VOF advection scheme and explicitly coupled with  
288    the two-phase Darcy model. Regarding the DBS method, the Navier-Stokes equation (NSE) is  
289    numerically solved within the Darcy-Brinkman model for the flow in both open fractures and  
290    continuum matrix domain by introducing the additional terms in the NSE equation [49, 71].

291    We firstly create a simple 2D geometry with one fracture within matrix (Fig. 9). This geometry  
292    being numerically discretised with respect to 'HybridPNM' (Fig. 10b) and DBS (Fig. 10a)  
293    models. The numerical mesh is irregular for 'Hybrid PNM' being geometrically different for  
294    fracture and matrix domains and contains 2640 cells. Besides, as can be observed in Fig. 10b,  
295    the 'HybridPNM' model contains only one adjacent matrix which is in line with the conceptual  
296    representation of this method introduced in Section 2 (Fig. 1). Nevertheless, the actual size of this  
297    adjacent matrix is equal to the total matrix volume presented in Fig. 9 being artificially decreased  
298    for visualisation purposes. In turn, the mesh is regular for DBS consisting of 6400 cuboid grid  
299    blocks. All demo 'HybridPNM' and DBS simulations with this geometry are conducted by using  
300    one core of Intel Core i5 processor.

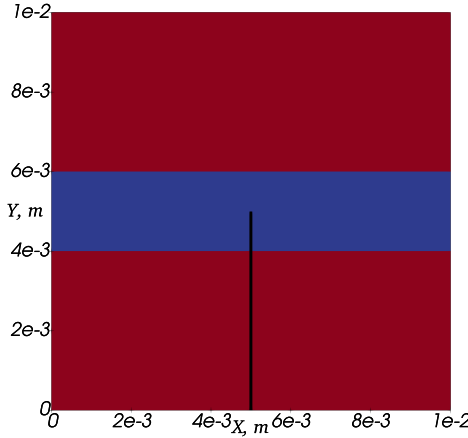


Figure 9: Synthetic geometry where blue domain represents a fracture within matrix (red domain). A central vertical line depicts a cross-section location used for drawing 1D plots (Figs. 13 and 15).

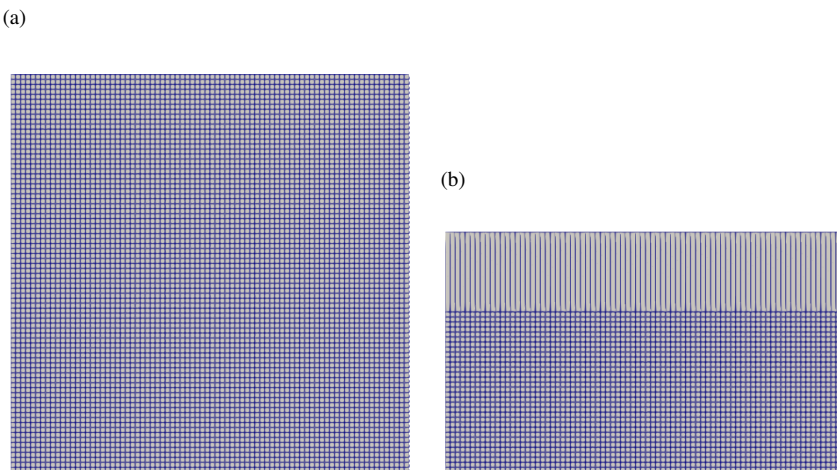


Figure 10: Numerical meshes used in cases 1-3: (a) DBS (6400 cells), (b) HybridPNM (2640 cells). The total volume of the adjacent matrix for 'HybridPNM' model is artificially reduced by half for visualisation purposes.

301 There are four demonstrative demo cases conducted throughout this section. In Table 1,  
 302 the physical phenomena involved in these demo simulations are summarised. Tables 2 and 3  
 303 list the realistic simulation parameters which are taken from a variety of available literature  
 304 sources. The presented demo cases exemplify the potential application of the 'HybridPNM'

solver for modelling absolute permeability variation due to matrix shrinkage-swellng (Case 1), gas adsorption to the coal matrix with respect to one-phase flow (Case 2) and two-phase flow (Cases 3 and 4).

Table 1: Physical characteristics of conducted simulations

Characteristics	Demo cases			
	1	2	3	4
Dimensions	2D			
Synthetic/Realistic (S/R)	S		R	
One-phase	+	-		
Two-phase	-		+	
Rock compressibility	+	-		
Sorption	+			

Table 2: Petrophysical characteristics and fluid properties

Parameter	Value
$\gamma^{*1}$	$7 \times 10^{-2} \text{ kg/s}^2$
$k^{*2} \text{ Case 2}$	$10^{-17} \text{ m}^2$
$k^{*2} \text{ Cases 3 \& 4}$	$10^{-19} \text{ m}^2$
$A_c$	0 Pa
$A_i, m_i, m_c$	I
$S_{ir}$	0
$\mu_l^{*3}$	$10^{-3} \text{ Pa s}$
$\mu_g^{*4}$	$10^{-5} \text{ Pa s}$
$\rho_l$	$10^3 \text{ kg/m}^3$
$\rho_g$	$24.6 \text{ kg/m}^3$

$*_1$  - [85];  $*_2$  - [3, 86, 87, 88];

$*_3$  - liquid;  $*_4$  - gas.

Table 3: Parameters of Langmuir and Palmer-Mansoori equations

Parameter	Value
$p_0$	$10^6 \text{ Pa}$
$E^{*1}$	$1.38 \times 10^9 \text{ Pa}$
$\phi_0^{*1}$	0.01
$\nu^{*1}$	0.35
$P_L^{*1}$	$2.1 \times 10^6 \text{ Pa}$
$\alpha_L^{*2}$	$230 \text{ kg/m}^3$
$\varepsilon_L^{*3}$	0.035

\*<sub>1</sub> - [89]; \*<sub>2</sub> - [90]; \*<sub>3</sub> - [91].

308 In Case 1, the Palmer-Mansoori model is embedded into the 'HybridPNM' numerical solution  
 309 by introducing the correction factor  $F_k$  (Eqs. 2 and 4) to absolute permeability. This allows us to  
 310 empirically account for the dependence between the absolute permeability of coal fractures and the  
 311 effective stress. In the Palmer-Mansoori model, both effective stress and sorption-induced stress  
 312 are taken into account. Thus, the resulting permeability variation depends upon the competition  
 313 between these two phenomena. A set of five one-phase simulations is conducted for realistic pore  
 314 pressures typically found in CSG reservoirs ranging between 0.5 - 4.5 MPa [92, 93]. The pressure  
 315 boundary conditions imposed at the inlet and outlet are the Dirichlet type. The relation between  
 316 the initial and current absolute permeability  $k/k_0$  is obtained both numerically ('HybridPNM')  
 317 and analytically (Eq. (3)) and depicted in Fig. 11. There is a close match between the numerically  
 318 obtained curve and the analytical solution (Fig. 11). The concave up shape of the curves reflects  
 319 the ongoing competition between fracture shrinkage and swelling.

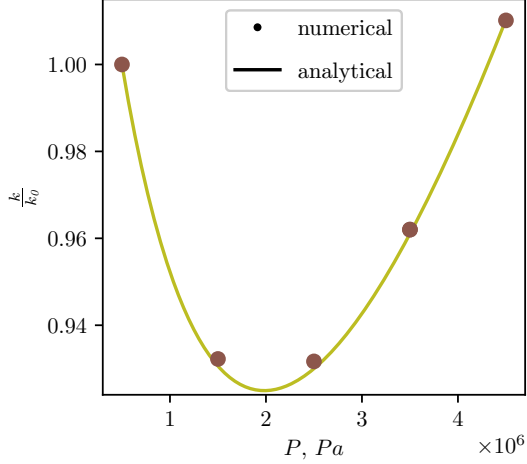


Figure 11: Case 1. Comparison between permeability variation numerically estimated by 'HybridPNM' and obtained by the Palmer-Mansoori analytical model for the pore pressures range of 0.5 - 4.5 MPa. Effective stress and sorption-induced stress are taken into account.

In Case 2, 'HybridPNM' and DBS one-phase simulations with gas adsorption are conducted  
 (Fig. 13). Both fracture and matrix domains initially contain gas while the adsorbed gas amount  
 is equal to its equilibrium value estimated via the Langmuir isotherm. The boundary conditions  
 are the Dirichlet type while there is no initial pressure gradient between the sample inlet and  
 outlet. The inlet and outlet pressure is then gradually increased in time which rapidly affects the  
 more conductive fracture. As a result, the gas adsorption firstly commences at the matrix regions  
 closest to the fracture and subsequently progresses inside the matrix. Moreover, the pressure  
 gradient between the fracture and coal matrix also leads to free gas advection. In Fig. 12, the  
 adsorbed gas concentration map is depicted at time  $10^3$  s for 'HybridPNM' and DBS simulations.  
 Likewise, the adsorbed gas concentration and pressure profile are depicted in Fig 13 at particular  
 cross-section (Fig. 9) of the 2D domain. As can be observed, the 'HybridPNM' and DBS outputs  
 closely coincide with respect to the depicted transient simulation parameters.

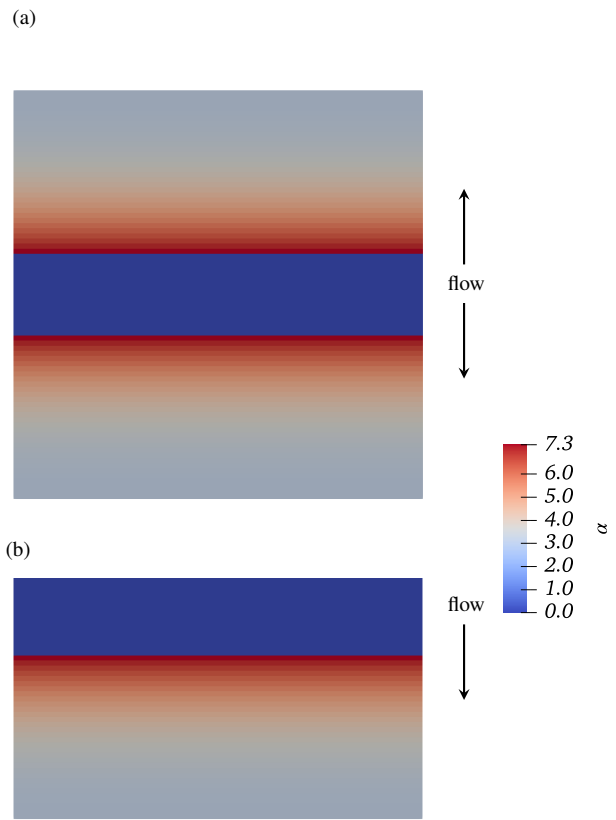


Figure 12: One-phase simulation. Adsorbed volume gas concentration at time  $10^3$ s : (a) DBS, (b) 'HybridPNM' multi-physics simulations.

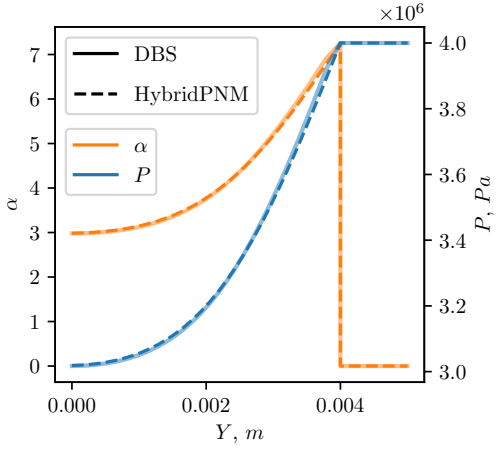


Figure 13: Pressure and volume concentration distribution along the  $Y$ -axis of 2D rectangular channel at time  $10^3$ s for DBS and 'HybridPNM' one-phase simulation with adsorption.

In Case 3, the fracture is initially filled with water while the matrix contains free and adsorbed gas. At initial conditions, the pressure inside the sample is uniform while adsorbed gas concentration is equal to its Langmuir equilibrium value. The boundary conditions for pressure in this simulation are the same as in Case 2. Once pressure is increased at the inlet and outlet, it rapidly distributes within the fracture and also increases in the matrix but at a significantly slower pace due to low matrix permeability (Table 2). An increase in pressure inside the matrix affects the equilibrium Langmuir gas concentration and gas commences adsorbing from a free state within the coal matrix. The gas adsorption process as well as the pressure gradient between the fracture and matrix allows water to interpenetrate the matrix and displace gas. In Fig. 14, the saturation distributions inside the sample is depicted for both 'HybridPNM' and DBS simulations. Clearly, the saturation maps closely coincide. Likewise, the adsorbed gas concentration and pressure profiles follow the same pattern and also closely match when comparing 'HybridPNM' and DBS outputs (Fig. 15).

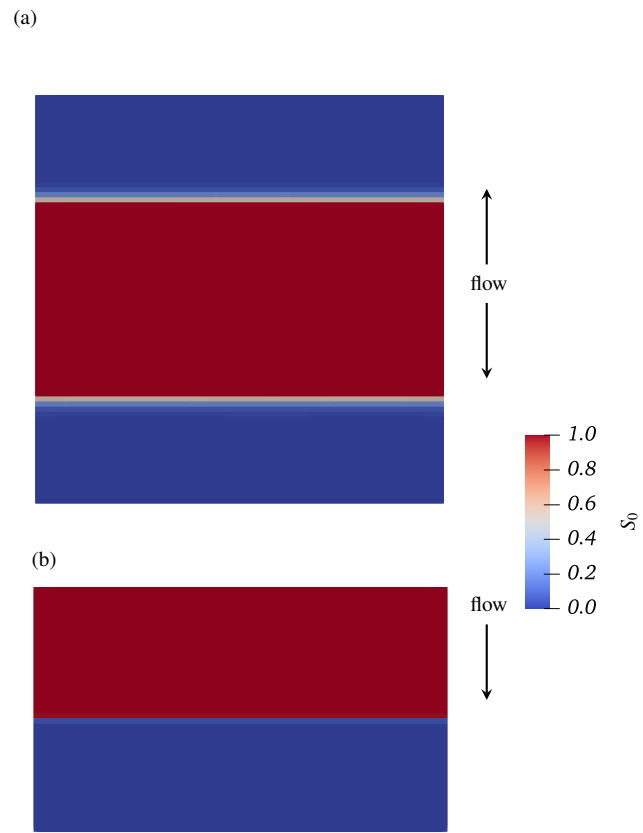


Figure 14: Two-phase simulation. Liquid saturation at time  $23s$  : (a) DBS, (b) 'HybridPNM' multi-physics simulations.

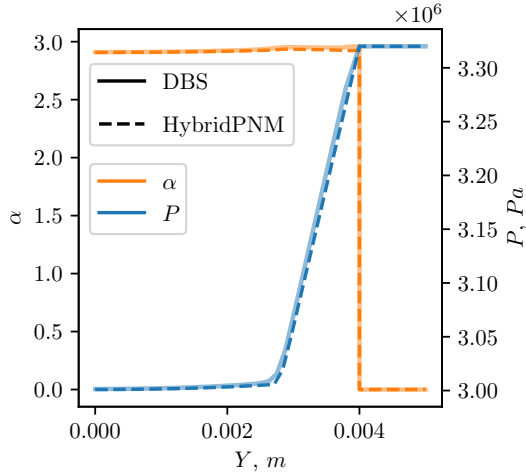


Figure 15: Pressure and volume concentration distribution along the  $Y$ -axis of 2D rectangular channel at time 23s for DBS and 'HybridPNM' two-phase simulation with adsorption.

Having the simulations conducted on a simple synthetic 2D geometry, we then use the 2D micro-CT image of coal with a developed network of connected cleats. Image dimensions are  $2001 \times 2501$  with resolution of  $28 \mu\text{m}$ . The details regarding the image segmentation routine can be found in [71] while the sample geographic origin and its petrophysical characteristics are described in [94].

The segmented micro-CT image is being used to extract the PN model for the 'HybridPNM' simulation (Fig. 16a). Here we use a simple semi-manual extraction algorithm which can be divided into two main steps: identifying all the cleats' intersection points and coordinates of the individual fractures; fitting cuboids into the void spaces of the micro-CT image to identify fractures' apertures. The segmented micro-CT image and extracted PN model are then discretised to conduct numerical simulations (Figs. 16b and 16c). The numerical 2D mesh of the 'HybridPNM' model consists of 73194 grid blocks while the DBS mesh being discretised consists of 412672 cells. The difference in the number of numerical cells between the 'HybridPNM' and DNS models would increase somewhat by one order of magnitude if 3D geometry was utilised.

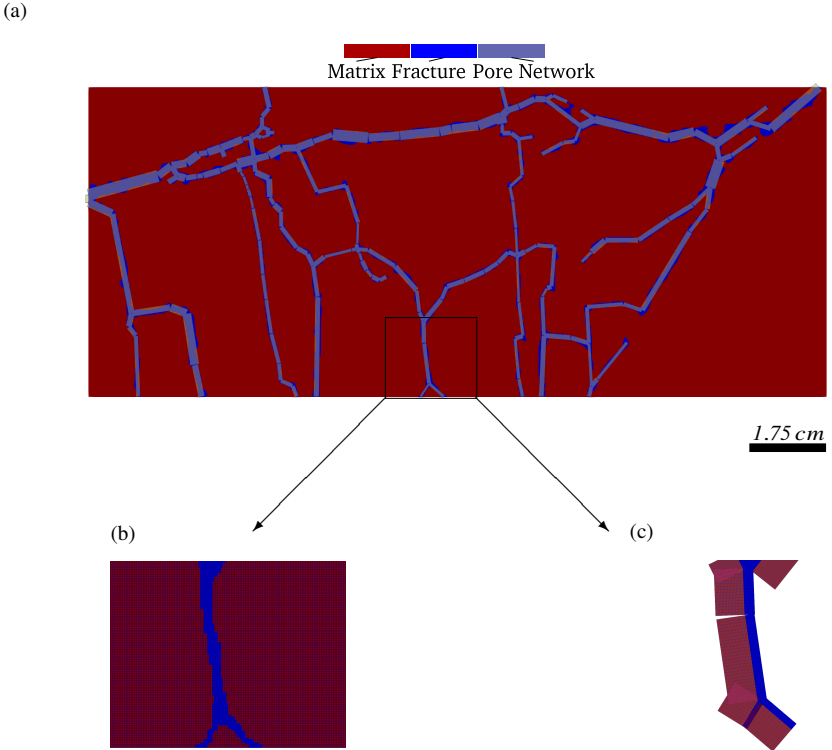
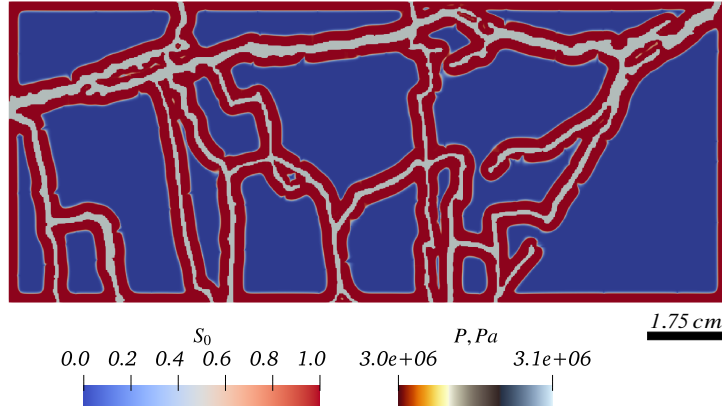


Figure 16: Numerical mesh generation: (a) pore network model of coal fractures with underlying micro-CT image, (b) DBS numerical mesh (412672 cells in total), (c) 'HybridPNM' grid-block topology (73194 cells in total).

359 In Case 4, the initial and boundary conditions as well as the multi-physics implemented are  
 360 similar to Case 3. The cleats are initially fully filled with water, the matrix contains free and  
 361 adsorbed gas while pressure across the sample is uniform. The pressure is then gradually increased  
 362 at the boundaries which results in a pressure gradient within a matrix-fracture system. The  
 363 pressure raise inside the cleats firstly affects the matrix regions adjacent to fracture which, in turn,  
 364 affects the Langmuir equilibrium gas concentration in these zones and provokes adsorption. The  
 365 adsorbed gas is displaced by water coming from the fractures and penetrates the matrix (Figs. 17a  
 366 and 17b).

(a)



(b)

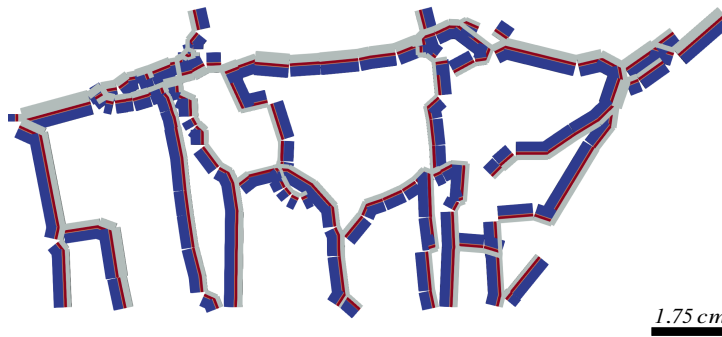


Figure 17: Pressure in fractures and water saturation in coal matrix for (a) DBS and (b) 'HybridPNM' simulations at time 5s. Execution times of 'HybridPNM' and DBS simulations are 571s and 23901s, respectively.

367 While the geometry of the DBS numerical mesh repeats the original segmented 2D image,  
 368 the 'HybridPNM' model operates on a mesh extracted with significant geometric simplifications  
 369 described in Section 2. As a result, Fig. 17 does not allow for visually comparing saturation maps  
 370 of the 'HybridPNM' and DBS models. To make such a comparison, we calculate three dynamic  
 371 flow characteristics for both solvers and compare them with respect to R-squared ( $R^2$ ) values. In  
 372 Fig. 18, the 'HybridPNM' and DBS simulations are compared concerning the average saturation,  
 373 adsorbed volume gas concentration, and average pressure inside the matrix in time. There is  
 374 an acceptable agreement within 4% between the 'HybridPNM' and reference DBS simulations  
 375 for all the characteristics calculated for comparative analysis. The best match ( $R^2 = 0.996$ ) is

376 achieved between the average pressure values  $P$  of 'HybridPNM' and DBS simulations (Fig. 18c)  
 377 while there is a slightly higher deviation between the two models with respect to saturation  $S_0$   
 378 (Fig. 18a,  $R^2 = 0.97$ ) and adsorbed gas concentration  $\alpha$  (Fig. 18b,  $R^2 = 0.96$ ). The shape of  
 379 the 'HybridPNM' curves is not as smooth as for the DBS simulations which can be explained  
 380 by a significant difference in approaches used for representing the topology of the matrix do-  
 381 main (Fig. 16). Nevertheless, the comparative study allows us to conclude that the geometric  
 382 and numerical simplifications used in the 'HybridPNM' solver allow to capture the transient flow  
 383 dynamics in the multi-scale multi-physics simulations on realistic micro-CT images of coal when  
 384 benchmarking against the complex DBS framework.

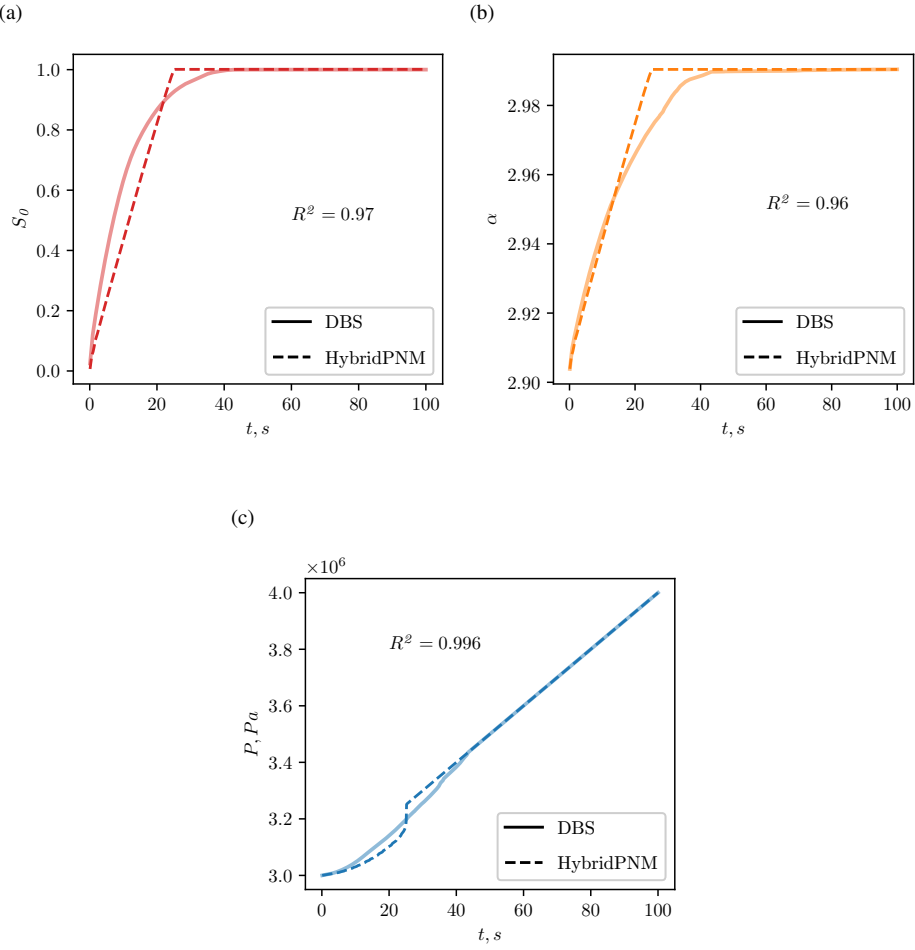


Figure 18: Comparison of DBS and 'HybridPNM' transient realistic simulations with respect to matrix average (a) water saturation, (b) volume gas concentration, and (c) pore pressure.

385 There are two main benefits which are desirable when utilising PNM-based pore-scale sim-  
386 ulations. Firstly, it is quite straightforward to incorporate various multi-physics phenomena in a  
387 mathematically simplified PNM numerical routine. This resulted in a vast number of research  
388 articles which use PNM in addressing the multi-physics flow in shale matrix [61, 63, 95, 96, 96].  
389 Secondly, such numerical simplifications, especially the usage of analytical solutions (e.g., Ha-  
390 gen–Poiseuille equation) of the NSE equations, allow us to reduce the computational time and  
391 make it possible to run the PNM-based simulations with an ordinary desktop PC. Despite the  
392 developed 'HybridPNM' model is not a typical PNM with respect to its numerical scheme and  
393 discretisation, it still benefits from the usage of the analytical Hagen–Poiseuille equation within  
394 its numerical model. In terms of computational time for a realistic 2D case, the 'HybridPNM'  
395 simulation is conducted with one core of Intel Core i5 processor and took 571s while the DBS  
396 computational routine used 50 cores of Intel Xeon Gold 6242R processor and took 23901s. The  
397 parallelisation of the DBS simulation is executed via Message Passing Interface (MPI) and by  
398 using the 'decomposePar' utility available in 'OpenFoam' [97]. As a result, the non-parallelised  
399 'HybridPNM' solver is 42 times faster for a 2D Case 4 than its DBS analogue. Such results  
400 open up a possibility to process the core-scale images of coal with the developed 'HybridPNM'  
401 model.

#### 402 4. Conclusion

403 The main goal of this paper is to demonstrate the applicability of the developed 'HybridPNM'  
404 model to capture various multi-scale multi-physics phenomena with respect to geologically com-  
405 plex coal seam formations. The utilised hybrid approach couples the pore-network based flow in  
406 fractures with the continuum Darcy model in the matrix. The 'HybridPNM' simulations were  
407 compared against the previously developed Darcy–Brinkman–Stokes (DBS) framework [71] and  
408 available analytical solutions. Studied phenomena include multi-scale multiphase flow in coal  
409 fractures and in the matrix, rock compressibility, sorption-induced swelling, as well as gas adsorp-  
410 tion within the coal matrix. There are two types of geometry used to conduct demo simulations  
411 throughout this study: simple synthetic and more complex realistic images of coal. The following  
412 observations can be drawn based on the conducted simulation study:

- 413 • The available analytical and empirical models can be easily introduced within the 'Hy-  
414 bridPNM' numerical scheme in order to account for the variation in coal porosity and

415 absolute permeability due to fracture shrinkage and swelling.

- 416 • The 'HybridPNM' and DBS simulations of one-phase and two-phase multi-phase flow  
417 with sorption closely coincide. For instance, comparing the outputs of 'HybridPNM' and  
418 DBS models, the  $R^2$  value computed for the realistic simulation has not exceeded 4% with  
419 respect to average saturation, adsorbed gas amount, and average pore pressure.
- 420 • The close match between 'HybridPNM' and DBS simulations allows us to conclude that  
421 geometric and numerical simplifications used in the developed PNM-based hybrid approach  
422 are justifiable.
- 423 • In terms of computational effort, the non-parallelised 'HybridPNM' solver is more than 40  
424 times faster than its parallelised DBS analogue for the complex realistic simulation. Such  
425 an achievement may allow to process of the core-scale images of coal with the developed  
426 'HybridPNM' model, especially with the aid of parallel computing.

427 Future work will be focused on the adaptation of the 'HybridPNM' solver to simulations  
428 concerning  $CO_2$  sequestration and hydrogen storage in coal seams. For this, the mechanism  
429 of competitive sorption will be embedded into the 'HybridPNM' numerical scheme via the  
430 multi-component adsorption.

## 431 References

- 432 [1] Q. Li, Y. Ju, Y. Bao, Z. Yan, X. Li, Y. Sun, Composition, origin, and distribution of coalbed methane in the huaipei  
433 coalfield, china, Energy & Fuels 29 (2) (2015) 546–555. doi:[10.1021/ef502132u](https://doi.org/10.1021/ef502132u).  
434 URL <https://pubs.acs.org/doi/10.1021/ef502132u>
- 435 [2] M. Faiz, L. Stalker, N. Sherwood, A. Saghafi, M. Wold, S. Barclay, J. Choudhury, W. Barker, I. Wang, Bio-  
436 enhancement of coal bed methane resources in the Southern Sydney Basin, The APPEA Journal 43 (1) (2003) 595.  
437 doi:[10.1071/AJ02033](https://doi.org/10.1071/AJ02033).  
438 URL <http://www.publish.csiro.au/?paper=AJ02033>
- 439 [3] T. A. Moore, Coalbed methane: A review, International Journal of Coal Geology 101 (2012) 36–81. doi:  
440 [10.1016/j.coal.2012.05.011](https://doi.org/10.1016/j.coal.2012.05.011).  
441 URL <https://linkinghub.elsevier.com/retrieve/pii/S0166516212001760>
- 442 [4] P. K. Singh, Geological and petrological considerations for coal bed methane exploration: A review, Energy  
443 Sources, Part A: Recovery, Utilization, and Environmental Effects 33 (13) (2011) 1211–1220. doi:[10.1080/15567030903330678](https://doi.org/10.1080/15567030903330678).  
444 URL <http://www.tandfonline.com/doi/abs/10.1080/15567030903330678>

- 446 [5] P. Mostaghimi, R. T. Armstrong, A. Gerami, Y. Hu, Y. Jing, F. Kamali, M. Liu, Z. Liu, X. Lu, H. L. Ramandi,  
 447 A. Zamani, Y. Zhang, Cleat-scale characterisation of coal: An overview, *Journal of Natural Gas Science and*  
 448 *Engineering* 39 (2017) 143–160. doi:[10.1016/j.jngse.2017.01.025](https://doi.org/10.1016/j.jngse.2017.01.025).  
 449 URL <https://linkinghub.elsevier.com/retrieve/pii/S1875510017300343>
- 450 [6] I. Hamawand, T. Yusaf, S. G. Hamawand, Coal seam gas and associated water: A review paper, *Renewable and*  
 451 *Sustainable Energy Reviews* 22 (2013) 550–560. doi:[10.1016/j.rser.2013.02.030](https://doi.org/10.1016/j.rser.2013.02.030).  
 452 URL <https://linkinghub.elsevier.com/retrieve/pii/S1364032113001329>
- 453 [7] S. Laubach, R. Marrett, J. Olson, A. Scott, Characteristics and origins of coal cleat: A review, *International Journal*  
 454 *of Coal Geology* 35 (1) (1998) 175–207. doi:[10.1016/S0166-5162\(97\)00012-8](https://doi.org/10.1016/S0166-5162(97)00012-8).  
 455 URL <https://linkinghub.elsevier.com/retrieve/pii/S0166516297000128>
- 456 [8] S. Karimpouli, P. Tahmasebi, H. L. Ramandi, A review of experimental and numerical modeling of digital coalbed  
 457 methane: Imaging, segmentation, fracture modeling and permeability prediction, *International Journal of Coal*  
 458 *Geology* 228 (2020) 103552. doi:[10.1016/j.coal.2020.103552](https://doi.org/10.1016/j.coal.2020.103552).  
 459 URL <https://linkinghub.elsevier.com/retrieve/pii/S0166516220305486>
- 460 [9] R. M. Flores, Coalbed methane: From hazard to resource, *International Journal of Coal Geology* 35 (1998) 3–26.  
 461 doi:[https://doi.org/10.1016/S0166-5162\(97\)00043-8](https://doi.org/10.1016/S0166-5162(97)00043-8).  
 462 URL <https://www.sciencedirect.com/science/article/pii/S0166516297000438>
- 463 [10] A. Salmachi, M. Rajabi, C. Wainman, S. Mackie, P. McCabe, B. Camac, C. Clarkson, History, geology, in situ  
 464 stress pattern, gas content and permeability of coal seam gas basins in australia: A review, *Energies* 14 (9) (2021)  
 465 2651. doi:[10.3390/en14092651](https://doi.org/10.3390/en14092651).  
 466 URL <https://www.mdpi.com/1996-1073/14/9/2651>
- 467 [11] S. Tao, S. Chen, Z. Pan, Current status, challenges, and policy suggestions for coalbed methane industry development  
 468 in china: A review, *Energy Science & Engineering* 7 (4) (2019) 1059–1074. doi:[10.1002/ese3.358](https://doi.org/10.1002/ese3.358).  
 469 URL <https://onlinelibrary.wiley.com/doi/10.1002/ese3.358>
- 470 [12] H. Jianchao, W. Zhiwei, L. Pingkuo, Current states of coalbed methane and its sustainability perspectives in china,  
 471 *International Journal of Energy Research* 42 (11) (2018) 3454–3476. doi:[10.1002/er.4085](https://doi.org/10.1002/er.4085).  
 472 URL <https://onlinelibrary.wiley.com/doi/10.1002/er.4085>
- 473 [13] I. Cronshaw, R. Quentin Grafton, A tale of two states: Development and regulation of coal bed methane extraction  
 474 in queensland and new south wales, australia, *Resources Policy* 50 (2016) 253–263. doi:[10.1016/j.resourpol.2016.10.007](https://doi.org/10.1016/j.resourpol.2016.10.007).  
 475 URL <https://linkinghub.elsevier.com/retrieve/pii/S0301420716300769>
- 476 [14] M. Mazzotti, R. Pini, G. Storti, Enhanced coalbed methane recovery, *The Journal of Supercritical Fluids* 47 (2009)  
 477 619–627. doi:<https://doi.org/10.1016/j.supflu.2008.08.013>.
- 478 [15] X. Li, Z.-m. Fang, Current status and technical challenges of CO<sub>2</sub> storage in coal seams and enhanced coalbed  
 479 methane recovery: an overview, *International Journal of Coal Science & Technology* 1 (1) (2014) 93–102. doi:  
 480 [10.1007/s40789-014-0002-9](https://doi.org/10.1007/s40789-014-0002-9).  
 481 URL <http://link.springer.com/10.1007/s40789-014-0002-9>
- 482 [16] Z. Pan, J. Ye, F. Zhou, Y. Tan, L. D. Connell, J. Fan, CO<sub>2</sub> storage in coal to enhance coalbed methane recovery:  
 483 a review of field experiments in china, *International Geology Review* 60 (5) (2018) 754–776. doi:[10.1080/00206814.2018.1442020](https://doi.org/10.1080/00206814.2018.1442020)

- 485        00206814.2017.1373607.
- 486        URL <https://www.tandfonline.com/doi/full/10.1080/00206814.2017.1373607>
- 487 [17] S. Iglauer, H. Abid, A. Al-Yaseri, A. Keshavarz, Hydrogen adsorption on sub-bituminous coal: Implications for  
488        hydrogen geo-storage, *Geophysical Research Letters* 48 (10) (2021). doi:[10.1029/2021GL092976](https://doi.org/10.1029/2021GL092976).
- 489        URL <https://onlinelibrary.wiley.com/doi/10.1029/2021GL092976>
- 490 [18] A. Keshavarz, H. Abid, M. Ali, S. Iglauer, Hydrogen diffusion in coal: Implications for hydrogen geo-storage,  
491        *Journal of Colloid and Interface Science* 608 (2022) 1457–1462. doi:[10.1016/j.jcis.2021.10.050](https://doi.org/10.1016/j.jcis.2021.10.050).
- 492        URL <https://linkinghub.elsevier.com/retrieve/pii/S0021979721017276>
- 493 [19] F. Bertrand, O. Buzzi, P. Bésuelle, F. Collin, Hydro-mechanical modelling of multiphase flow in naturally fractured  
494        coalbed using a multiscale approach, *Journal of Natural Gas Science and Engineering* 78 (2020) 103303. doi:  
495        [10.1016/j.jngse.2020.103303](https://doi.org/10.1016/j.jngse.2020.103303).
- 496        URL <https://linkinghub.elsevier.com/retrieve/pii/S1875510020301578>
- 497 [20] L. D. Connell, M. Lu, Z. Pan, An analytical coal permeability model for tri-axial strain and stress conditions,  
498        *International Journal of Coal Geology* 84 (2) (2010) 103–114. doi:[10.1016/j.coal.2010.08.011](https://doi.org/10.1016/j.coal.2010.08.011).
- 499        URL <https://linkinghub.elsevier.com/retrieve/pii/S0166516210001631>
- 500 [21] A. Busch, Y. Gensterblum, CBM and CO<sub>2</sub>-ECBM related sorption processes in coal: A review, *International  
501        Journal of Coal Geology* 87 (2) (2011) 49–71. doi:[10.1016/j.coal.2011.04.011](https://doi.org/10.1016/j.coal.2011.04.011).
- 502        URL <https://linkinghub.elsevier.com/retrieve/pii/S0166516211001200>
- 503 [22] J. Li, S. McDougall, K. Sorbie, Dynamic pore-scale network model (PNM) of water imbibition in porous media,  
504        *Advances in Water Resources* 107 (2017) 191–211. doi:[10.1016/j.advwatres.2017.06.017](https://doi.org/10.1016/j.advwatres.2017.06.017).
- 505        URL <https://linkinghub.elsevier.com/retrieve/pii/S0309170816304687>
- 506 [23] V. Joekar-Niasar, S. M. Hassanzadeh, Analysis of fundamentals of two-phase flow in porous media using dynamic  
507        pore-network models: A review, *Critical Reviews in Environmental Science and Technology* 42 (18) (2012) 1895–  
508        1976. doi:[10.1080/10643389.2011.574101](https://doi.org/10.1080/10643389.2011.574101).
- 509        URL <http://www.tandfonline.com/doi/abs/10.1080/10643389.2011.574101>
- 510 [24] M. S. Al-Gharbi, M. J. Blunt, Dynamic network modeling of two-phase drainage in porous media, *Physical Review  
511        E* 71 (1) (2005) 016308. doi:[10.1103/PhysRevE.71.016308](https://doi.org/10.1103/PhysRevE.71.016308).
- 512        URL <https://link.aps.org/doi/10.1103/PhysRevE.71.016308>
- 513 [25] P.-E. Oren, S. Bakke, O. Arntzen, Extending predictive capabilities to network models, *SPE Journal* 3 (4) (1998)  
514        324–336. doi:[10.2118/52052-PA](https://doi.org/10.2118/52052-PA).
- 515        URL <https://onepetro.org/SJ/article/3/04/324/170264/Extending-Predictive-Capabilities-to-Network>
- 516 [26] J. E. McClure, Z. Li, M. Berrill, T. Ramstad, The LBPM software package for simulating multiphase flow  
517        on digital images of porous rocks, *Computational Geosciences* 25 (3) (2021) 871–895. doi:[10.1007/s10596-020-10028-9](https://doi.org/10.1007/s10596-020-10028-9).
- 518        URL <https://link.springer.com/10.1007/s10596-020-10028-9>
- 519 [27] C. H. Arns, P. M. Adler, Fast laplace solver approach to pore-scale permeability, *Physical Review E* 97 (2) (2018)  
520        023303. doi:[10.1103/PhysRevE.97.023303](https://doi.org/10.1103/PhysRevE.97.023303).
- 521        URL <https://link.aps.org/doi/10.1103/PhysRevE.97.023303>
- 522 [28] D. Koroteev, O. Dinariev, N. Evseev, D. Klemin, A. Nadeev, S. Safonov, O. Gurpinar, S. Berg, C. van Kruijsdijk,

- 524 R. Armstrong, M. T. Myers, L. Hathon, H. de Jong, Direct hydrodynamic simulation of multiphase flow in porous  
 525 rock, *Petrophysics* 55 (3) (2014) 294–303.
- 526 URL <https://onepetro.org/petrophysics/article/55/04/294/171367/>  
 527 *Direct-Hydrodynamic-Simulation-of-Multiphase-Flow*
- 528 [29] A. Q. Raeini, M. J. Blunt, B. Bijeljic, Direct simulations of two-phase flow on micro-CT images of porous media and  
 529 upscaling of pore-scale forces, *Advances in Water Resources* 74 (2014) 116–126. doi:[10.1016/j.advwatres.2014.08.012](https://doi.org/10.1016/j.advwatres.2014.08.012).
- 530 URL <https://linkinghub.elsevier.com/retrieve/pii/S0309170814001730>
- 531 [30] V. Shabro, C. Torres-Verdín, F. Javadpour, K. Sepehrnoori, Finite-difference approximation for fluid-flow simulation  
 532 and calculation of permeability in porous media, *Transport in Porous Media* 94 (3) (2012) 775–793. doi:  
 533 [10.1007/s11242-012-0024-y](https://doi.org/10.1007/s11242-012-0024-y).
- 534 URL <http://link.springer.com/10.1007/s11242-012-0024-y>
- 535 [31] T. Bultreys, W. De Boever, V. Cnudde, Imaging and image-based fluid transport modeling at the pore scale in  
 536 geological materials: A practical introduction to the current state-of-the-art, *Earth-Science Reviews* 155 (2016)  
 537 93–128. doi:[10.1016/j.earscirev.2016.02.001](https://doi.org/10.1016/j.earscirev.2016.02.001).
- 538 URL <https://linkinghub.elsevier.com/retrieve/pii/S0012825216300150>
- 539 [32] R. Song, Y. Wang, S. Sun, J. Liu, Characterization and microfabrication of natural porous rocks: From micro-CT  
 540 imaging and digital rock modelling to micro-3d-printed rock analogs, *Journal of Petroleum Science and Engineering*  
 541 205 (2021) 108827. doi:[10.1016/j.petrol.2021.108827](https://doi.org/10.1016/j.petrol.2021.108827).
- 542 URL <https://linkinghub.elsevier.com/retrieve/pii/S0920410521004885>
- 543 [33] A. P. Sheppard, R. M. Sok, H. Averdunk, Techniques for image enhancement and segmentation of tomographic  
 544 images of porous materials, *Physica A: Statistical Mechanics and its Applications* 339 (1) (2004) 145–151. doi:  
 545 [10.1016/j.physa.2004.03.057](https://doi.org/10.1016/j.physa.2004.03.057).
- 546 URL <https://linkinghub.elsevier.com/retrieve/pii/S037843710400370X>
- 547 [34] A. Rabbani, M. Babaei, F. Javadpour, A triple pore network model (t-PNM) for gas flow simulation in fractured,  
 548 micro-porous and meso-porous media, *Transport in Porous Media* (2020). doi:[10.1007/s11242-020-01409-w](https://doi.org/10.1007/s11242-020-01409-w).
- 549 URL <http://link.springer.com/10.1007/s11242-020-01409-w>
- 550 [35] J. Gostick, Z. Khan, T. Tranter, M. Kok, M. Agnaou, M. Sadeghi, R. Jervis, PoreSpy: A python toolkit for  
 551 quantitative analysis of porous media images, *Journal of Open Source Software* 4 (37) (2019) 1296. doi:[10.21105/joss.01296](https://doi.org/10.21105/joss.01296).
- 552 URL <http://joss.theoj.org/papers/10.21105/joss.01296>
- 553 [36] H. Dong, M. J. Blunt, Pore-network extraction from micro-computerized-tomography images, *Physical Review E*  
 554 80 (3) (2009) 036307. doi:[10.1103/PhysRevE.80.036307](https://doi.org/10.1103/PhysRevE.80.036307).
- 555 URL <https://link.aps.org/doi/10.1103/PhysRevE.80.036307>
- 556 [37] H. Gan, S. Nandi, P. Walker, Nature of the porosity in american coals, *Fuel* 51 (4) (1972) 272–277. doi:  
 557 [10.1016/0016-2361\(72\)90003-8](https://doi.org/10.1016/0016-2361(72)90003-8).
- 558 URL <https://linkinghub.elsevier.com/retrieve/pii/0016236172900038>
- 559 [38] K. Zhang, Y. Cheng, L. Wang, J. Dong, C. Hao, J. Jiang, Pore morphology characterization and its effect on methane  
 560 desorption in water-containing coal: An exploratory study on the mechanism of gas migration in water-injected coal

- 563 seam, Journal of Natural Gas Science and Engineering 75 (2020) 103152. doi:[10.1016/j.jngse.2020.103152](https://doi.org/10.1016/j.jngse.2020.103152).
- 564 URL <https://linkinghub.elsevier.com/retrieve/pii/S1875510020300068>
- 565 [39] X. Lu, R. T. Armstrong, P. Mostaghimi, Analysis of gas diffusivity in coal using micro-computed tomography, Fuel 261 (2020) 116384. doi:[10.1016/j.fuel.2019.116384](https://doi.org/10.1016/j.fuel.2019.116384).
- 566 URL <https://linkinghub.elsevier.com/retrieve/pii/S0016236119317387>
- 567 [40] C. Karacan, E. Okandan, Adsorption and gas transport in coal microstructure: investigation and evaluation by quantitative x-ray CT imaging, Fuel 80 (4) (2001) 509–520. doi:[https://doi.org/10.1016/S0016-2361\(00\)00112-5](https://doi.org/10.1016/S0016-2361(00)00112-5).
- 568 [41] Q. Xiong, T. G. Baychev, A. P. Jivkov, Review of pore network modelling of porous media: Experimental characterisations, network constructions and applications to reactive transport, Journal of Contaminant Hydrology 192 (2016) 101–117. doi:[10.1016/j.jconhyd.2016.07.002](https://doi.org/10.1016/j.jconhyd.2016.07.002).
- 569 URL <https://linkinghub.elsevier.com/retrieve/pii/S016977221630122X>
- 570 [42] T. Bultreys, L. Van Hoorebeke, V. Cnudde, Multi-scale, micro-computed tomography-based pore network models to simulate drainage in heterogeneous rocks, Advances in Water Resources 78 (2015) 36–49. doi:[10.1016/j.advwatres.2015.02.003](https://doi.org/10.1016/j.advwatres.2015.02.003).
- 571 URL <https://linkinghub.elsevier.com/retrieve/pii/S0309170815000299>
- 572 [43] Z. Lanetc, A. Zhuravljov, A. Shapoval, R. T. Armstrong, P. Mostaghimi, Inclusion of Microporosity in Numerical Simulation of Relative Permeability Curves, Vol. Day 1 Mon, February 21, 2022 of IPTC International Petroleum Technology Conference, 2022, p. 14. doi:[10.2523/IPTC-21975-MS](https://doi.org/10.2523/IPTC-21975-MS).
- 573 URL <https://doi.org/10.2523/IPTC-21975-MS>
- 574 [44] F. J. Carrillo, C. Soulaine, I. C. Bourg, The impact of sub-resolution porosity on numerical simulations of multiphase flow, Advances in Water Resources (2022) 104094doi:[10.1016/j.advwatres.2021.104094](https://doi.org/10.1016/j.advwatres.2021.104094).
- 575 URL <https://linkinghub.elsevier.com/retrieve/pii/S0309170821002451>
- 576 [45] F. Yang, A. G. Stack, V. Starchenko, Micro-continuum approach for mineral precipitation, Scientific Reports 11 (1) (2021) 3495. doi:[10.1038/s41598-021-82807-y](https://doi.org/10.1038/s41598-021-82807-y).
- 577 URL <http://www.nature.com/articles/s41598-021-82807-y>
- 578 [46] C. Soulaine, H. A. Tchelepi, Micro-continuum approach for pore-scale simulation of subsurface processes, Transport in Porous Media 113 (3) (2016) 431–456. doi:[10.1007/s11242-016-0701-3](https://doi.org/10.1007/s11242-016-0701-3).
- 579 URL <http://link.springer.com/10.1007/s11242-016-0701-3>
- 580 [47] J. You, K. J. Lee, Pore-scale study to analyze the impacts of porous media heterogeneity on mineral dissolution and acid transport using darcy–brinkmann–stokes method, Transport in Porous Media 137 (3) (2021) 575–602. doi:[10.1007/s11242-021-01577-3](https://doi.org/10.1007/s11242-021-01577-3).
- 581 URL <https://link.springer.com/10.1007/s11242-021-01577-3>
- 582 [48] D. H. Kang, E. Yang, T. S. Yun, Stokes-brinkman flow simulation based on 3-d  $\mu$ -CT images of porous rock using grayscale pore voxel permeability, Water Resources Research 55 (5) (2019) 4448–4464. doi:[10.1029/2018WR024179](https://doi.org/10.1029/2018WR024179).
- 583 URL <https://onlinelibrary.wiley.com/doi/abs/10.1029/2018WR024179>
- 584 [49] F. J. Carrillo, I. C. Bourg, C. Soulaine, Multiphase flow modeling in multiscale porous media: An open-source micro-continuum approach, Journal of Computational Physics: X 8 (2020) 100073. doi:[10.1016/j.jcp.2020.100073](https://doi.org/10.1016/j.jcp.2020.100073).
- 585 URL <https://doi.org/10.1016/j.jcp.2020.100073>

- 602       **100073.**
- 603       URL <https://linkinghub.elsevier.com/retrieve/pii/S2590055220300251>
- 604       [50] K. Singh, How hydraulic properties of organic matter control effective liquid permeability of mudrocks, Transport  
605       in Porous Media 129 (3) (2019) 761–777. doi:[10.1007/s11242-019-01305-y](https://doi.org/10.1007/s11242-019-01305-y).
- 606       URL <http://link.springer.com/10.1007/s11242-019-01305-y>
- 607       [51] T. D. Scheibe, W. A. Perkins, M. C. Richmond, M. I. McKinley, P. D. J. Romero-Gomez, M. Oostrom, T. W.  
608       Wietsma, J. A. Serkowski, J. M. Zachara, Pore-scale and multiscale numerical simulation of flow and transport in  
609       a laboratory-scale column, Water Resources Research 51 (2) (2015) 1023–1035. doi:[10.1002/2014WR015959](https://doi.org/10.1002/2014WR015959).  
610       URL <http://doi.wiley.com/10.1002/2014WR015959>
- 611       [52] F. Golfier, D. Lasseux, M. Quintard, Investigation of the effective permeability of vuggy or fractured porous  
612       media from a darcy-brinkman approach, Computational Geosciences 19 (1) (2015) 63–78. doi:[10.1007/s10596-014-9448-5](https://doi.org/10.1007/s10596-014-9448-5)  
613       URL <http://link.springer.com/10.1007/s10596-014-9448-5>
- 614       [53] M. A. Knackstedt, C. H. Arns, A. Ghous, A. Sakellariou, T. J. Senden, A. P. Sheppard, M. Sok, V. Nguyen, W. V.  
615       Pinczewski, 3d imaging and characterization of the pore space of carbonate core; implications to single and two  
616       phase flow properties, Society of Petrophysicists and Well-Log Analysts, 2006, p. 15.
- 617       [54] W. Zhao, Y. Cheng, Z. Pan, K. Wang, S. Liu, Gas diffusion in coal particles: A review of mathematical models and  
618       their applications, Fuel 252 (2019) 77–100. doi:[10.1016/j.fuel.2019.04.065](https://doi.org/10.1016/j.fuel.2019.04.065).  
619       URL <https://linkinghub.elsevier.com/retrieve/pii/S0016236119306209>
- 620       [55] M. M. Mohanty, B. K. Pal, Sorption behavior of coal for implication in coal bed methane an overview, International  
621       Journal of Mining Science and Technology 27 (2) (2017) 307–314. doi:[10.1016/j.ijmst.2017.01.014](https://doi.org/10.1016/j.ijmst.2017.01.014).  
622       URL <https://linkinghub.elsevier.com/retrieve/pii/S2095268617300605>
- 623       [56] J. Gao, H. Xing, L. Turner, K. Steel, M. Sedek, S. D. Golding, V. Rudolph, Pore-scale numerical investigation  
624       on chemical stimulation in coal and permeability enhancement for coal seam gas production, Transport in Porous  
625       Media 116 (1) (2017) 335–351. doi:[10.1007/s11242-016-0777-9](https://doi.org/10.1007/s11242-016-0777-9).  
626       URL <http://link.springer.com/10.1007/s11242-016-0777-9>
- 627       [57] E. P. Robertson, A permeability model for coal and other fractured, sorptive-elastic media, SPE Journal (2008) 11.
- 628       [58] J.-Q. Shi, S. Durucan, A model for changes in coalbed permeability during primary and enhanced methane recovery,  
629       SPE Reservoir Evaluation & Engineering 8 (4) (2005) 291–299. doi:[10.2118/87230-PA](https://doi.org/10.2118/87230-PA).  
630       URL <http://www.onepetro.org/doi/10.2118/87230-PA>
- 631       [59] W. Song, J. Yao, D. Wang, Y. Li, H. Sun, Y. Yang, Dynamic pore network modelling of real gas transport in shale  
632       nanopore structure, Journal of Petroleum Science and Engineering 184 (2020) 106506. doi:[10.1016/j.petrol.2019.106506](https://doi.org/10.1016/j.petrol.2019.106506).  
633       URL <https://linkinghub.elsevier.com/retrieve/pii/S0920410519309271>
- 634       [60] H. Yu, Y. Zhu, X. Jin, H. Liu, H. Wu, Multiscale simulations of shale gas transport in micro/nano-porous shale  
635       matrix considering pore structure influence, Journal of Natural Gas Science and Engineering 64 (2019) 28–40.  
636       doi:[10.1016/j.jngse.2019.01.016](https://doi.org/10.1016/j.jngse.2019.01.016).  
637       URL <https://linkinghub.elsevier.com/retrieve/pii/S1875510019300241>
- 638       [61] X. Huang, K. W. Bandilla, M. A. Celia, Multi-physics pore-network modeling of two-phase shale matrix flows,  
639

- 641 Transport in Porous Media 111 (1) (2016) 123–141. doi:[10.1007/s11242-015-0584-8](https://doi.org/10.1007/s11242-015-0584-8).
- 642 URL <http://link.springer.com/10.1007/s11242-015-0584-8>
- 643 [62] D. Wang, J. Yao, Z. Chen, W. Song, H. Sun, Multiphase flow model from pores to cores in organic-rich shale,  
644 Journal of Petroleum Science and Engineering 194 (2020) 107317. doi:[10.1016/j.petrol.2020.107317](https://doi.org/10.1016/j.petrol.2020.107317).  
645 URL <https://linkinghub.elsevier.com/retrieve/pii/S0920410520303934>
- 646 [63] Y. Yang, K. Wang, L. Zhang, H. Sun, K. Zhang, J. Ma, Pore-scale simulation of shale oil flow based on pore network  
647 model, Fuel 251 (2019) 683–692. doi:[10.1016/j.fuel.2019.03.083](https://doi.org/10.1016/j.fuel.2019.03.083).  
648 URL <https://linkinghub.elsevier.com/retrieve/pii/S0016236119304570>
- 649 [64] A. Mehmani, M. Prodanović, The application of sorption hysteresis in nano-petrophysics using multiscale multi-  
650 physics network models, International Journal of Coal Geology 128-129 (2014) 96–108. doi:[10.1016/j.coal.2014.03.008](https://doi.org/10.1016/j.coal.2014.03.008).  
651 URL <https://linkinghub.elsevier.com/retrieve/pii/S0166516214000706>
- 652 [65] Z. Lanetc, A. Zhuravljov, Y. Jing, R. T. Armstrong, P. Mostaghimi, Coupling of transient matrix diffusion and  
653 pore network models for gas flow in coal, Journal of Natural Gas Science and Engineering 88 (2021) 103741.  
654 doi:[10.1016/j.jngse.2020.103741](https://doi.org/10.1016/j.jngse.2020.103741).  
655 URL <https://linkinghub.elsevier.com/retrieve/pii/S1875510020305953>
- 656 [66] Y. Jing, A. Rabbani, R. T. Armstrong, J. Wang, P. Mostaghimi, A hybrid fracture-micropore network model for  
657 multiphysics gas flow in coal, Fuel 281 (2020) 118687. doi:[10.1016/j.fuel.2020.118687](https://doi.org/10.1016/j.fuel.2020.118687).  
658 URL <https://linkinghub.elsevier.com/retrieve/pii/S0016236120316835>
- 659 [67] F. J. Carrillo, I. C. Bourg, Modeling multiphase flow within and around deformable porous materials: A darcy-  
660 brinkman-biot approach, Water Resources Research 57 (2) (2021). doi:[10.1029/2020WR028734](https://doi.org/10.1029/2020WR028734).  
661 URL <https://onlinelibrary.wiley.com/doi/10.1029/2020WR028734>
- 662 [68] S. Molins, C. Soulaine, N. I. Prasianakis, A. Abbasi, P. Poncet, A. J. C. Ladd, V. Starchenko, S. Roman, D. Trebotich,  
663 H. A. Tchelepi, C. I. Steefel, Simulation of mineral dissolution at the pore scale with evolving fluid-solid interfaces:  
664 review of approaches and benchmark problem set, Computational Geosciences 25 (4) (2021) 1285–1318. doi:  
665 [10.1007/s10596-019-09903-x](https://doi.org/10.1007/s10596-019-09903-x).  
666 URL <https://link.springer.com/10.1007/s10596-019-09903-x>
- 667 [69] C. Noiriel, C. Soulaine, Pore-scale imaging and modelling of reactive flow in evolving porous media: Tracking  
668 the dynamics of the fluid–rock interface, Transport in Porous Media 140 (1) (2021) 181–213. doi:[10.1007/s11242-021-01613-2](https://doi.org/10.1007/s11242-021-01613-2).  
669 URL <https://link.springer.com/10.1007/s11242-021-01613-2>
- 670 [70] F. J. Carrillo, I. C. Bourg, A darcy-brinkman-biot approach to modeling the hydrology and mechanics of porous  
671 media containing macropores and deformable microporous regions, Water Resources Research 55 (10) (2019)  
672 8096–8121. doi:[10.1029/2019WR024712](https://doi.org/10.1029/2019WR024712).  
673 URL <https://onlinelibrary.wiley.com/doi/10.1029/2019WR024712>
- 674 [71] Z. Lanetc, A. Zhuravljov, R. T. Armstrong, P. Mostaghimi, Multi-scale modelling of multi-physics flow in coal  
675 seams, Fuel (2022) 30.
- 676 [72] Z. Lanetc, A. Zhuravljov, Y. Jing, R. T. Armstrong, P. Mostaghimi, Coupling of pore network modelling and volume  
677 of fluid methods for multiphase flow in fractured media, Fuel 319 (2022) 123563. doi:[10.1016/j.fuel.2022.123563](https://doi.org/10.1016/j.fuel.2022.123563).  
678 URL <https://linkinghub.elsevier.com/retrieve/pii/S0016236122003563>

- 680           123563.
- 681           URL <https://linkinghub.elsevier.com/retrieve/pii/S0016236122004288>
- 682       [73] Z. Lanetc, A. Zhuravljov, R. T. Armstrong, P. Mostaghimi, Accuracy of transient multi-phase simulations in fractured  
683       media by hybrid VOF-PNM method, *Fuel* (2022) 23.
- 684       [74] R. Cornish, Flow in a pipe of rectangular cross-section, *Proceedings of the Royal Society of London. Series A,  
685       Containing Papers of a Mathematical and Physical Character* 120 (786) (1928) 691–700.
- 686       [75] I. Palmer, J. Mansoori, How permeability depends on stress and pore pressure in coalbeds: A new model, *SPE  
687       Annual Technical Conference and Exhibition, SPE*, 1996, p. 8. doi:<https://doi.org/10.2118/36737-MS>.
- 688           URL <https://onepetro.org/SPEATCE/proceedings-abstract/96SPE/All-96SPE/SPE-36737-MS/>  
689       59035
- 690       [76] C. R. Clarkson, Z. Pan, I. Palmer, S. Harpalani, Predicting Sorption-Induced Strain and Permeability Increase  
691       With Depletion for Coalbed-Methane Reservoirs, *SPE Journal* 15 (01) (2010) 152–159. doi:[10.2118/114778-PA](https://doi.org/10.2118/114778-PA).  
692           URL <https://onepetro.org/SJ/article/15/01/152/192001/Predicting-Sorption-Induced-Strain-and>
- 693       [77] K. Aziz, Petroleum reservoir simulation, *Applied Science Publishers* 476 (1979).
- 694       [78] R. Yang, S. Liu, H. Wang, Z. Lun, X. Zhou, C. Zhao, C. Min, H. Zhang, Y. Xu, D. Zhang, Influence of h<sub>2</sub> o  
695       on adsorbed CH<sub>4</sub> on coal displaced by CO<sub>2</sub> injection: Implication for CO<sub>2</sub> sequestration in coal seam with  
696       enhanced CH<sub>4</sub> recovery (CO<sub>2</sub>-ECBM), *Industrial & Engineering Chemistry Research* 60 (43) (2021) 15817–  
697       15833. doi:[10.1021/acs.iecr.1c03099](https://doi.org/10.1021/acs.iecr.1c03099)  
698           URL <https://pubs.acs.org/doi/10.1021/acs.iecr.1c03099>
- 699       [79] I. Klewiah, D. S. Berawala, H. C. A. Walker, P. Ø. Andersen, P. H. Nadeau, Review of experimental sorption studies  
700       of co2 and ch4 in shales, *Journal of Natural Gas Science and Engineering* 73 (2020) 103045.
- 701       [80] T. Gang, M. Kelkar, History matching for determination of fracture permeability and capillary pressure, *SPE  
702       Reservoir Evaluation & Engineering* 11 (05) (2008) 813–822.
- 703       [81] R. H. Brooks, *Hydraulic properties of porous media*, Colorado State University, 1965.
- 704       [82] A. Zhuravljov, Z. Lanetc, Relevance of analytical Buckley–Leverett solution for immiscible oil displacement  
705       by various gases, *Journal of Petroleum Exploration and Production Technology* 9 (1) (2019) 617–626. doi:  
706       [10.1007/s13202-018-0516-6](https://doi.org/10.1007/s13202-018-0516-6).  
707           URL <http://link.springer.com/10.1007/s13202-018-0516-6>
- 708       [83] H. J. Welge, A simplified method for computing oil recovery by gas or water drive, *Journal of Petroleum Technology*  
709       4 (4) (1952) 91–98. doi:[10.2118/124-G](https://doi.org/10.2118/124-G).  
710           URL <https://onepetro.org/JPT/article/4/04/91/161892/A-Simplified-Method-for-Computing-Oil-Recovery-by>
- 711       [84] S. E. Buckley, M. Leverett, Mechanism of fluid displacement in sands, *Transactions of the AIME* 146 (01) (1942)  
712       107–116.
- 713       [85] H.-B. Qin, Z.-Y. Zhang, C.-Y. Sun, G.-J. Chen, Q.-L. Ma, Z.-F. Ning, Interfacial Tension between Methane and  
714       Water Containing Kinetic Hydrate Inhibitor PVP Ramification and Its Emulsification Property, *Journal of Chemical  
715       & Engineering Data* 62 (9) (2017) 2770–2775. doi:[10.1021/acs.jced.7b00113](https://doi.org/10.1021/acs.jced.7b00113).  
716           URL <https://pubs.acs.org/doi/10.1021/acs.jced.7b00113>
- 717       [86] D. Viete, P. Ranjith, The effect of CO<sub>2</sub> on the geomechanical and permeability behaviour of brown coal: Implications  
718       for coal seam CO<sub>2</sub> sequestration, *International Journal of Coal Geology* 66 (3) (2006) 204–216. doi:[10.1016/j.intjocoalgeol.2006.02.001](https://doi.org/10.1016/j.intjocoalgeol.2006.02.001).

- 719       coal.2005.09.002.
- 720       URL <https://linkinghub.elsevier.com/retrieve/pii/S0166516205001527>
- 721 [87] F. Han, A. Busch, B. M. Krooss, Z. Liu, N. van Wageningen, J. Yang, Experimental Study on Fluid Transport  
722 Processes in the Cleat and Matrix Systems of Coal, *Energy & Fuels* 24 (12) (2010) 6653–6661. doi:[10.1021/ef100165w](https://doi.org/10.1021/ef100165w).
- 723       URL <https://pubs.acs.org/doi/10.1021/ef100165w>
- 724 [88] M.-Y. Wei, J. Liu, Y.-K. Liu, Z.-H. Liu, D. Elsworth, Effect of adsorption-induced matrix swelling on coal  
725 permeability evolution of micro-fracture with the real geometry, *Petroleum Science* 18 (4) (2021) 1143–1152.  
726 doi:[10.1016/j.petsci.2021.07.006](https://doi.org/10.1016/j.petsci.2021.07.006).
- 727       URL <https://linkinghub.elsevier.com/retrieve/pii/S199582262100011X>
- 728 [89] E. P. Robertson, R. L. Christiansen, Modeling Laboratory Permeability in Coal Using Sorption-Induced-Strain  
729 Data, *SPE Reservoir Evaluation & Engineering* 10 (03) (2007) 260–269. doi:[10.2118/97068-PA](https://doi.org/10.2118/97068-PA).
- 730       URL <https://onepetro.org/REE/article/10/03/260/196860/Modeling-Laboratory-Permeability-in-Coal-Using>
- 731 [90] E. Fan, S. Tang, C. Zhang, Q. Guo, C. Sun, Methane Sorption Capacity of Organics and Clays in High-Over Matured  
732 Shale-Gas Systems, *Energy Exploration & Exploitation* 32 (6) (2014) 927–942. doi:[10.1260/0144-5987.32.6.927](https://doi.org/10.1260/0144-5987.32.6.927).
- 733       URL <http://journals.sagepub.com/doi/10.1260/0144-5987.32.6.927>
- 734 [91] S. Peng, Z. Fang, J. Shen, J. Xu, G. Wang, Effects of gas sorption-induced swelling/shrinkage on the cleat  
735 compressibility of coal under different bedding directions, *Scientific Reports* 7 (1) (2017) 14337. doi:[10.1038/s41598-017-14678-1](https://doi.org/10.1038/s41598-017-14678-1).
- 736       URL <http://www.nature.com/articles/s41598-017-14678-1>
- 737 [92] Y. Qin, T. A. Moore, J. Shen, Z. Yang, Y. Shen, G. Wang, Resources and geology of coalbed methane in china: a  
738 review, *International Geology Review* 60 (5) (2018) 777–812. doi:[10.1080/00206814.2017.1408034](https://doi.org/10.1080/00206814.2017.1408034).
- 739       URL <https://www.tandfonline.com/doi/full/10.1080/00206814.2017.1408034>
- 740 [93] M. Pillalamarry, S. Harpalani, S. Liu, Gas diffusion behavior of coal and its impact on production from coalbed  
741 methane reservoirs, *International Journal of Coal Geology* 86 (4) (2011) 342–348. doi:[10.1016/j.coal.2011.03.007](https://doi.org/10.1016/j.coal.2011.03.007).
- 742       URL <https://linkinghub.elsevier.com/retrieve/pii/S0166516211000619>
- 743 [94] D. Shaw, P. Mostaghimi, R. T. Armstrong, The dynamic behaviour of coal relative permeability curves, *Fuel* 253  
744 (2019) 293–304. doi:[10.1016/j.fuel.2019.04.107](https://doi.org/10.1016/j.fuel.2019.04.107).
- 745       URL <https://linkinghub.elsevier.com/retrieve/pii/S0016236119306738>
- 746 [95] R. Cui, Q. Feng, H. Chen, W. Zhang, S. Wang, Multiscale random pore network modeling of oil-water two-phase  
747 slip flow in shale matrix, *Journal of Petroleum Science and Engineering* 175 (2019) 46–59. doi:[10.1016/j.petrol.2018.12.026](https://doi.org/10.1016/j.petrol.2018.12.026).
- 748       URL <https://linkinghub.elsevier.com/retrieve/pii/S0920410518311124>
- 749 [96] P. Zhang, L. Hu, J. N. Meegoda, S. Gao, Micro/nano-pore network analysis of gas flow in shale matrix, *Scientific  
750 Reports* 5 (1) (2015) 13501. doi:[10.1038/srep13501](https://doi.org/10.1038/srep13501).
- 751       URL <http://www.nature.com/articles/srep13501>
- 752 [97] C. J. Greenshields, Openfoam user guide version 6, The OpenFOAM Foundation (2018) 237.